Bibliographical reference

Physical and Spurious Modes in Mixed Finite Element Formulation for the Galbrun Equation, Felix Dietzsch, Luis Hervella-Nieto, Steffen Marburg, Rodolfo Rodríguez and Hannah Weisbecker, Acta Acustica **vol. 100** (Number 3), 2014, pp. 493-512

DOI

https://doi.org/10.3813/AAA.918730

Acta Acustica united with Acustica
Vol. 100 (2014) 493 – 512

DOI 10.3813/AAA.918730

Physical and Spurious Modes in Mixed Finite Element Formulation for the Galbrun Equation

Felix Dietzsch[1)], Luis Hervella-Nieto[2)], Steffen Marburg[3)], Rodolfo Rodríguez[4)], Hannah Weisbecker[5)]

[1)] Institut für Energieverfahrenstechnik, Chemieingenieurwesen, TU Bergakademie, Freiberg, Germany

[2)] Facultade de Informática, Universidade de A Coruña, A Coruña, Spain

[3)] LRT4 – Institute of Mechanics, Universität der Bundeswehr München, 85579 Neubiberg, Germany. steffen.marburg@unibw.de

[4)] CI^{2}MA, Departamento de Ingeniería Matemática, Universidad de Concepción, Concepción, Chile

[5)] Institut für Festkörpermechanik, Technische Universität Dresden, 01062 Dresden, Germany

Summary

Sound propagation in moving media can be described by the Galbrun equation for the oscillating component of the fluid displacement. A displacement based finite element formulation using standard Lagrangian elements produces spurious modes, which renders it unfeasible for any numerical purpose. Herein, the quadratic eigenvalue problem for the mixed formulation in 2D using Mini elements and Taylor-Hood elements is set up and solved. Solution confirms that both element types are suitable for low Mach numbers and under certain conditions. Although the formulation is not free from spurious results, it is shown that physical and spurious modes are well separated for low Mach numbers in non-dissipative systems. Vorticity modes, such as those arising from the linearized Euler equations, could not be identified. If absorbing walls are considered, separation of physical and spurious modes becomes less clear. Then, eigenvalues of both types of modes are located closer to each other in the complex plane. Examples include the one-dimensional duct problem, for which the spurious modes are discussed for the energy conserving problem, and an annular duct under two conditions: first subjected to a shear flow and with a rigid boundary, and secondly with an absorbing boundary, which allows investigating the dissipative case.

PACS no. 43.29.Py

1. Introduction

For many aeroacoustic problems such as jet noise, duct acoustics and liner design, a main focus lies on the prediction of sound propagation in nonuniform flow, see for example [1, 2]. Mathematically, such problems are often described by the linear Euler equations (LEE) and by the Acoustic Perturbation Equations (APE), see for example [3, 4, 5] for LEE and [6, 7, 5] for APE. However, acoustic problems with ambient flow can also be modeled using the Galbrun equation, which was first derived by Galbrun in 1931 [8]. This is a second order linear partial differential equation describing the sound propagation in terms of a displacement perturbation as the only variable. It is an advantage of the Galbrun equation, that an exact expression for acoustic energy and intensity [9] exists. Furthermore, boundary conditions and coupling conditions with structures are easily formulated [10] since both, structure and fluid, are described by the displacement. The Galbrun equation is the result of a simplification of sound propagation in an arbitrary inviscid flow [11].

Received 5 July 2013,
accepted 4 January 2014.

For practical use, a mixed formulation in terms of displacement and pressure perturbation is used. Despite using these two variables for a solution, there is still a gain of variables compared to the conventional system of equations since LEE require introduction of variables for velocity, pressure and entropy. The solution of the eigenvalue problem of the Galbrun equation can help to better understand the phenomenon of sound propagation in the presence of ambient flow. Especially in the case of swirling mean flows, the Galbrun formulation seems to be an interesting alternative since an often used simplification of the LEE, the so called full-potential formulation, is not applicable. A few papers [12, 13, 14, 10, 15, 16, 17, 18] deal with solving Galbrun equation using the finite element method (FEM). However, none of these works explicitly addresses the solution of the eigenvalue problem. On the other hand, Brazier [19] derived eigenvalues of the free field Galbrun equation. The solution predicts acoustical and vorticity modes, where the latter are rotational modes which are divergence free. Hence, the sound pressure of vorticity modes is zero. Similar to the acoustic modes, eigenvalues of vorticity modes are predicted to be real. Among other applications, solution of the eigenvalue problem is relevant for intonation of musical woodwind instruments. While traditionally analyzed only experimentally, application of numerical methods has been approaching this class of instruments in recent years. Two examples of these applications to woodwind instruments are those by Fuß *et al.* [20] for the recorder and by Richter *et al.* [21] for the bassoon.

In this study, the quadratic eigenvalue problem resulting from discretization of the Galbrun equation is solved using FEM. A mixed element formulation is chosen. This formulation is known to satisfy the inf-sup condition in the no-flow case. Although there have been indications that this formulation reliably suppresses spurious modes even in the presence of inviscid flow, satisfaction of the inf-sup condition by these formulations for non-vanishing flow has not been proved so far. Treyssède *et al.* [13] showed that spurious modes are not observed when Mini elements or Taylor-Hood elements are used. The paper by Gabard *et al.* [16] indicates that spurious modes can be observed for Mini elements at large Mach numbers, in particular for Mach numbers greater than 0.5. Taylor-Hood elements performed more stable even at large Mach numbers. It remained unclear whether these formulations are actually free of spurious modes or not. The authors of this article could not find any indication in the literature where the eigenvalue problem of Galbrun equation has been investigated for a finite element model.

In this study, it is demonstrated why Taylor-Hood elements perform well for weakly damped problems. Previous results for Mini elements are confirmed and, for higher Mach numbers, real eigenvalues of spurious character are evaluated. Nevertheless, spurious modes are found in all cases except for the no-flow case. For Taylor-Hood elements, these eigenvalues occur in regions far (enough) away from the real axis. Furthermore, it is shown that problems with large regions of absorption (e.g., exterior acoustic problems) do not easily allow the separation between physical and spurious modes. In these cases, special techniques are required to identify the relevant physical modes.

The outline of the paper is as follows. The Galbrun equation is recalled in section 2. Then, a mixed formulation of the corresponding eigenvalue problem is given. This section ends with a brief description of the finite elements used to solve this problem. In section 3, the sound propagation inside a one-dimensional duct with rigid walls is examined. A constant ambient pressure and a steady ambient flow velocity are assumed. In this case, the analytical solution is known and this allows the effectiveness of the used finite element methods to be assessed. A shear flow problem inside an annulus accounts for the test case in section 4. Again, only rigid boundary conditions are considered. The annulus with partially absorbing boundary conditions is solved as a third test in section 5. In spite of the bounded character of the domain, the configuration of this test is similar to that of an exterior problem. Finally, in section 6 some conclusions are drawn.

2. Theoretical aspects

2.1. Galbrun equation

The equation for an acoustic problem with ambient flow in terms of the oscillatory displacement $\boldsymbol{w}$, also referred to as the Galbrun equation, can be written as [9, 11]

$$\rho_0 \frac{\mathrm{d}^2 \boldsymbol{w}}{\mathrm{d}t^2} + \left(\nabla \cdot \boldsymbol{w} + \boldsymbol{w} \cdot \nabla\right) \nabla p_0 - \nabla\left(\rho_0 {c_0}^2 \nabla \cdot \boldsymbol{w} + \boldsymbol{w} \cdot \nabla p_0\right) = \mathbf{0}. \tag{1}$$

Herein, p_0, ρ_0, and c_0 represent the ambient pressure, mass density and speed of sound, respectively. A detailed discussion on the derivation of the Galbrun equation can be found in [9] and [22].

For numerical analysis, the values of the ambient variables p_0, ρ_0, and c_0, are assumed to be constant. This simplifies the Galbrun equation to

$$\rho_0 \frac{d^2 \boldsymbol{w}}{dt^2} - \rho_0 {c_0}^2 \nabla\left(\nabla \cdot \boldsymbol{w}\right) = \mathbf{0}. \tag{2}$$

Note that $d\boldsymbol{w}/dt$ accounts for the material time derivative which is determined as

$$\frac{\mathrm{d}(\cdot)}{\mathrm{d}t} = \frac{\partial(\cdot)}{\partial t} + \boldsymbol{v}_0 \cdot \nabla(\cdot), \tag{3}$$

where a steady ambient flow velocity $\boldsymbol{v}_0$ has been assumed. For constant speed of sound c_0 and constant ambient density ρ_0, equation (2) looks similar to the Pierce equation for the velocity potential [23]. However, the Pierce equation is a generalized scalar wave equation whereas the simplified Galbrun equation remains a vector equation. The Mach number as normalized velocity is related to the ambient flow velocity and the speed of sound as

$$Ma = \frac{|\boldsymbol{v}_0|}{c_0}. \tag{4}$$

Furthermore, a harmonic time dependence $\mathrm{e}^{-\mathrm{i}\omega t}$ is assumed for oscillatory quantities, in particular for the displacement $\boldsymbol{w}$ and for the (sound) pressure p. Application of harmonic time dependence to equation (2) yields

$$-\rho_0 \omega^2 \boldsymbol{w} - 2\mathrm{i}\omega \rho_0 \boldsymbol{v}_0 \cdot \nabla \boldsymbol{w} + \rho_0 \boldsymbol{v}_0 \cdot \nabla\left(\boldsymbol{v}_0 \cdot \nabla \boldsymbol{w}\right) - \rho_0 {c_0}^2 \nabla\left(\nabla \cdot \boldsymbol{w}\right) = \mathbf{0}. \tag{5}$$

If not mentioned otherwise, a rigid surface boundary condition will be regarded in the numerical simulation. At a motionless and rigid surface the normal component of the oscillatory displacement has to vanish, i.e.,

$$\boldsymbol{w} \cdot \boldsymbol{n} = 0, \tag{6}$$

where $\boldsymbol{n}$ is the unit outward normal. The implementation of this boundary condition for the Galbrun equation is quite simple, because the displacement is an explicit variable.

In the second numerical example of this study, an admittance boundary condition is applied to consider the effect of absorption. Assuming constant ambient pressure, a boundary admittance Y, and vanishing flow in the direction normal to the boundary (i.e., $\boldsymbol{v}_0 \cdot \boldsymbol{n} = 0$), the admittance boundary condition can be formulated as

$$-\mathrm{i}\omega \boldsymbol{w} \cdot \boldsymbol{n} = Yp = \frac{\tilde{Y}p}{\rho_0 c_0}, \tag{7}$$

where $\tilde{Y}$ represents a normalized boundary admittance. A detailed discussion of different boundary conditions can be found in [9].

2.2. Weak formulation and polynomial eigenvalue problem

It has been shown in the paper by Treyssède *et al.* [13] that a simple weak formulation of equation (5) produces spurious modes when Lagrangian elements are used. To avoid these spurious modes, a mixed finite element formulation was proposed. This mixed formulation is based on the two variables, pressure and displacement, which satisfy the inf-sup condition in the no-flow case. Then, the mixed formulation, which is an analogous formulation to equation (5), can be written as

$$\begin{aligned} -\rho_0\omega^2 \boldsymbol{w} - 2\mathrm{i}\omega\rho_0 \boldsymbol{v}_0 \cdot \nabla \boldsymbol{w} & \\ +\rho_0 \boldsymbol{v}_0 \cdot \nabla\big(\boldsymbol{v}_0 \cdot \nabla \boldsymbol{w}\big)\nabla p &= \boldsymbol{0}, \\ p + \rho_0 c_0^2 \nabla \cdot \boldsymbol{w} &= 0. \end{aligned} \tag{8}$$

To obtain a variational form of equation (8), test functions $\boldsymbol{w}^*$ and p^* are introduced. The result of the weak formulation as given in [13] assumes a divergence-free flow field $\boldsymbol{v}_0$, i.e., $\nabla \cdot \boldsymbol{v}_0 = 0$. With the domain Ω and the boundary Γ, integration by parts leads to the weak formulation of the Galbrun equation:

$$\begin{aligned} &-\int_\Omega \frac{1}{\rho_0 {c_0}^2} p^* p \,\mathrm{d}\Omega + \int_\Omega \nabla p^* \cdot \boldsymbol{w} \,\mathrm{d}\Omega \\ &+ \int_\Omega \boldsymbol{w}^* \cdot \nabla p \,\mathrm{d}\Omega - \omega^2 \int_\Omega \rho_0 \boldsymbol{w}^* \cdot \boldsymbol{w} \,\mathrm{d}\Omega \\ &- \mathrm{i}\omega \int_\Omega \rho_0 \boldsymbol{w}^* \cdot \big(\boldsymbol{v}_0 \cdot \nabla \boldsymbol{w}\big) \,\mathrm{d}\Omega \\ &+ \mathrm{i}\omega \int_\Omega \rho_0 \big(\boldsymbol{v}_0 \cdot \nabla \boldsymbol{w}^*\big) \cdot \boldsymbol{w} \,\mathrm{d}\Omega \\ &- \int_\Omega \rho_0 \big(\boldsymbol{v}_0 \cdot \nabla \boldsymbol{w}^*\big) \cdot \big(\boldsymbol{v}_0 \cdot \nabla \boldsymbol{w}\big) \,\mathrm{d}\Omega \\ &+ \int_\Gamma \boldsymbol{w}^* \cdot \left[\rho_0 \big(\boldsymbol{v}_0 \cdot \boldsymbol{n}\big) \frac{\mathrm{d}\boldsymbol{w}}{\mathrm{d}t}\right] \mathrm{d}\Gamma \\ &- \int_\Gamma p^* \big(\boldsymbol{w} \cdot \boldsymbol{n}\big) \,\mathrm{d}\Gamma = 0, \qquad \forall \big\{\boldsymbol{w}^*, p^*\big\}. \end{aligned} \tag{9}$$

The first four terms represent the no-flow case, the following three are added in the ambient flow case, and the last two are the boundary integrals appearing due to integration by parts. The terms with ω^2 and ω will later lead to the mass and damping matrices, respectively, and the remaining integrals contribute to the stiffness matrix. Up to this point, the left-hand side of equation (9) results in a quadratic polynomial matrix.

In computations with flow limited to domains with rigid walls and absorbing walls with zero flow in the normal direction, the normal components of the ambient flow $\boldsymbol{v}_0 \cdot \boldsymbol{n}$ are equal to zero on the boundary. Hence, the first boundary integral vanishes in such a case. The second boundary integral of equation (9) vanishes for rigid boundary conditions (cf. equation 6). Frequency dependence of the boundary admittance controls whether the contribution of the second boundary integral is added to the mass, stiffness or damping matrix, or even if it results in a new term. For instance, a frequency independent boundary admittance results in a matrix proportional to $1/\omega$. Thus, in this case, the polynomial matrix becomes cubic (cf. equation (11), below).

In the case of rigid walls, equation (9) results in a quadratic eigenvalue problem as

$$-\omega^2 \boldsymbol{M}\boldsymbol{u} - \mathrm{i}\omega \boldsymbol{D}\boldsymbol{u} + \boldsymbol{K}\boldsymbol{u} = \boldsymbol{0}, \tag{10}$$

with $\boldsymbol{u}$ comprising displacement and pressure degrees of freedom. The mass matrix $\boldsymbol{M}$ and the stiffness matrix $\boldsymbol{K}$ are symmetric and real, the damping matrix $\boldsymbol{D}$ is skew-symmetric. In this mixed formulation, both, the mass and damping matrices, are singular because neither of them include entries connected to the pressure terms. The eigenvalues of this problem occur either as real values or as conjugate complex pairs. Consequently, the distribution of eigenvalues in the complex plane should be symmetric with respect to the real axis.

In case of frequency independent admittance boundary conditions, equation (9) results in a cubic eigenvalue problem as

$$-\omega^3 \boldsymbol{M}\boldsymbol{u} - \mathrm{i}\omega^2 \boldsymbol{D}\boldsymbol{u} + \omega \boldsymbol{K}\boldsymbol{u} + \boldsymbol{A}\boldsymbol{u} = \boldsymbol{0}. \tag{11}$$

Matrices $\boldsymbol{M}$, $\boldsymbol{D}$ and $\boldsymbol{K}$ are the same as in the case of rigid walls. Usually, $\boldsymbol{A}$ is sparse and complex.

The eigenvalue problem is set up and solved by using the commercial codes COMSOL Multiphysics [24] or MATLAB [25], by means of the commands `femeig` and `polyeig`, respectively. The former is based on the implicitly restarted Arnoldi method (IRAM), which provides a certain number of eigenvalues around a complex shift value. The latter is a variant of QZ method adapted to polynomial eigenvalue problems. The default tolerance has been used in both cases: machine precision $\epsilon \approx 2 \times 10^{-16}$.

2.3. Types of finite elements

Herein, different types of finite elements are investigated. Their choice is mainly motivated by the selection of finite elements in the papers by Treyssède *et al.* [13] and Gabard *et al.* [16]. Behavior of standard Lagrangian elements is demonstrated for comparison only. The discussion of elements is limited to the two-dimensional case. However, all of these element types are known for three dimensional applications as well. In what follows, elements will be referred to by their names and by abbreviations as used in [16] and are shown in Figure 1.

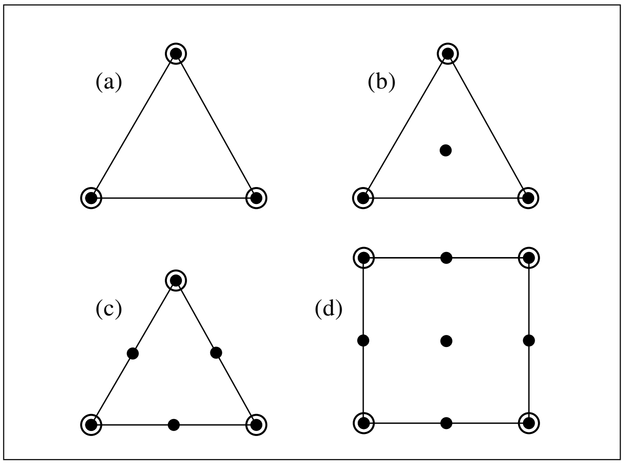

Figure 1. Element types used to solve the eigenvalue problem. (a) Linear element, T3–3c, (b) Mini element, T4–3c, (c) Taylor-Hood el., T6–3c, (d) Taylor-Hood el., T9–4c. •: Displacement dof, ○: Pressure dof.

2.3.1. Lagrangian elements

Standard Lagrangian elements are well-known. They represent the most commonly used type of finite elements; see for example [26, 27]. Herein, only linear triangular elements as shown in Figure 1a are used. All nodes of the element are equipped with displacement and pressure degrees of freedom. This element type will be referred to as T3–3c.

Bonnet–Ben Dhia *et al.* [28, 29, 30] also used Lagrangian elements for the displacement formulation, but applying an additional penalty term to damp out spurious modes. The influence of such a penalty term is not considered in this paper.

2.3.2. Mini elements

Similar to Lagrangian elements, Mini elements are triangular elements with displacement and pressure degrees of freedom at their three vertices (cf. Figure 1b). In addition to these nine degrees of freedom, another two degrees of freedom for the displacement are linked with a fourth node in the barycenter of the element. The associated basis functions are known as bubble functions since they vanish along all edges of the element. The abbreviation for this element is T4–3c.

2.3.3. Taylor-Hood elements

A combination of linear approximation for pressure and quadratic approximation for displacement is known as the Taylor-Hood element. Treyssède *et al.* [13] and Gabard *et al.* [16] tested quadrilateral elements as shown in Figure 1d. To achieve a better comparison with the triangular Mini elements, triangular Taylor-Hood elements are tested as well (cf. Figure 1c). As shown, the Taylor-Hood elements will be referred to as T6–3c and Q9–4c.

2.3.4. Other elements

For this study, the authors have tested a number of additional higher order elements similar to Taylor-Hood-like elements, e.g. T10–6c and Q25–16c. Since they behave similar to the Taylor-Hood elements shown in Figures 1c and 1d, a detailed description of these test cases is omitted.

A similar approach was discussed by Beriot [31]. He extended the approach in [15, 16] to hierarchical elements (*hp*–FEM). In particular, the authors tested the displacement formulation and the mixed-formulation. In both cases, it was shown that higher order polynomials improve the stability of the method.

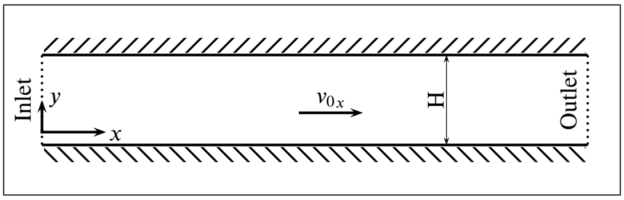

Figure 2. Geometry of the duct.

3. Computational example I: The long duct

3.1. Model description

A similar example as in [32] (for the no-flow case) is considered. It consists of a fluid-filled duct of length L and width H such that $H \ll L$. It is assumed that the duct domain covers the area of $0 \leq x \leq L$ and $0 \leq y \leq H$ (cf. Figure 2). The ambient flow velocity $\boldsymbol{v}_0$ reduces to a (positive) component v_{0x}, whereas the orthogonal component vanishes: $v_{0y} = 0$. Then, the Mach number is $Ma = v_{0x}/c_0$. Since solutions of the two-dimensional method are compared with the analytical solution of the corresponding one-dimensional problem, it is necessary to apply zero boundary conditions to all surfaces as in equation (6). Moreover, at the inlet and at the outlet, both the normal and the tangential displacement components are forced to be zero [13] such that $\boldsymbol{w}(x = 0) = \boldsymbol{w}(x = L) = \boldsymbol{0}$.

3.2. Analytical solution

It is possible to derive an analytical solution of the Galbrun equation for a one-dimensional duct with constant ambient velocity [33] (see [34, 5] for other similar problems). The mixed formulation of the simplified Galbrun equation (8) for the one-dimensional case when the y component of $\boldsymbol{w}$ vanishes (i.e., $\boldsymbol{w} = (w, 0)$) and p and w do not depend on y reads as follows

$$\begin{aligned} -\rho_0\omega^2 w - 2\mathrm{i}\omega\rho_0 v_0 w' + \rho_0 v_0 (v_0 w')' + p' &= 0, \\ p + \rho_0 c_0^2 w' &= 0, \end{aligned} \tag{12}$$

where v_0 is a flow field with vanishing y-component. It is easy to return to the displacement formulation which yields

$$\omega^2 w + 2\mathrm{i}\omega v_0 w' + (c_0^2 - v_0^2) w'' = 0. \tag{13}$$

Equation (13) describes the sound propagation in a duct. An infinite duct has a continuous spectrum of eigenvalues. In order to have a mathematically well posed problem with a discrete spectrum, the problem is solved on the interval $(0, L)$ with the boundary conditions $w_x(0) = 0$ and $w_x(L) = 0$. In this case, these boundary conditions do not represent actual rigid walls, which would physically contradict the condition of a constant velocity, but they correspond to nodal points imposed by the eigenfunctions. Although the resulting problem is not physically realistic, it will allow to derive useful information. (The experiments reported in the subsequent sections have instead a clear physical character). Notice that under these boundary conditions, the boundary term $\int_\Gamma \boldsymbol{w}^* \cdot \left[\rho_0(\boldsymbol{v}_0 \cdot \boldsymbol{n})\frac{d\boldsymbol{w}}{dt}\right] d\Gamma$ from equation (9) does not appear either, because the test functions $\boldsymbol{w}^*$ vanish on the inlet and the outlet of the duct. Thus, a discrete spectrum of eigenvectors with wavelengths $\lambda = 2L, 3/2L, L, L/2, \ldots$ is extracted from the original continuous spectrum. The eigenvalues for the circular frequency ω_n and the frequency f_n are real and yield

$$\omega_n = \frac{c_0 \pi n}{L}\left(1 - Ma^2\right), \quad \text{i.e.,} \quad f_n = \frac{c_0 n}{2L}\left(1 - Ma^2\right). \tag{14}$$

The solution corresponds to that of the no-flow case diminished by the term Ma^2. The first three eigenfrequencies as functions of the Mach number are depicted in Figure 3.

Contrary to the eigenvalues, the eigenvectors are complex:

$$w_n = C\left[\mathrm{e}^{-\mathrm{i}\frac{\pi n}{c_0 L}(v_{0x}+c_0)x} - \mathrm{e}^{-\mathrm{i}\frac{\pi n}{c_0 L}(v_{0x}-c_0)x}\right]. \tag{15}$$

It is easy to show that ω_n (cf. equation 14) and w_n (cf. equation 15) are indeed solutions of the one-dimensional Galbrun equation (13).

Here and below, C is chosen in such a way that the first real maximum amplitude on the domain equals 1. The behavior of the real and imaginary parts are depicted in Figure 4. Their amplitudes increase and decrease periodically. Notice that real and imaginary parts exhibit the same behavior shifted in phase.

3.3. Numerical results

In this subsection, it will be clarified whether the elements, depicted in Figure 1, are suitable to solve the eigenvalue problem or if it is necessary to look for alternative elements. It turns out that the applicability of elements strongly depends on the Mach number. This behavior has already been noticed in former studies [13, 10, 14, 12, 15], but none of these explicitly addresses the eigenvalue problem; the main focus within their studies was on the propagation of acoustic waves. Herein, a classification of the elements will show at which Mach numbers each of them can be reasonably employed. In what follows, an element is denoted to be *stable* if the exact solutions (cf. equation 14) can be clearly identified in the numerical spectrum. Otherwise, if the field of regular solutions is polluted by parasitic values, the element is defined to be *unstable*.

The domain used for this study has a length of 3.4 m and its width is set to 0.05 m. This high ratio of side lengths is chosen to maximize the number of regular modes which are only related to the length of the duct. The speed of

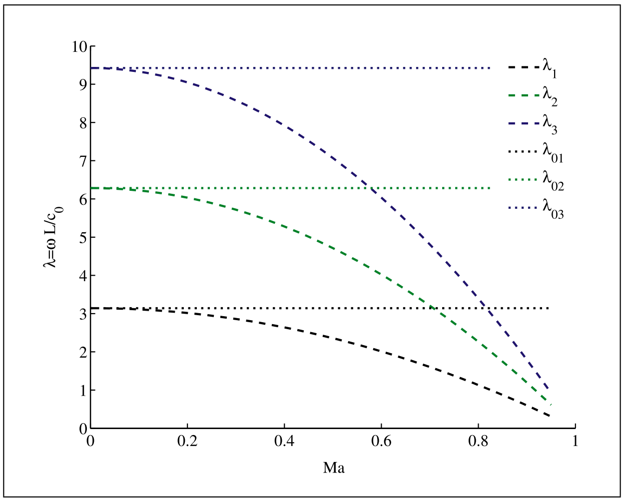

Figure 3. Duct: First three eigenfrequencies in terms of Ma.

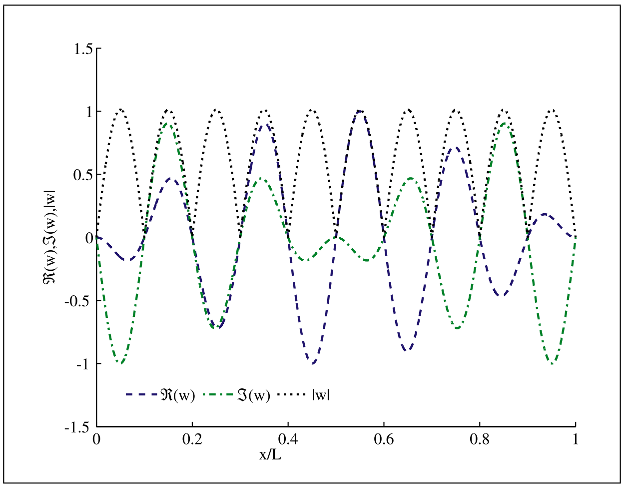

Figure 4. Duct: Behavior of $\Re(w_x)$ and $\Im(w_x)$ along the duct.

sound and mass density are assumed to be $c_0 = 340\,\mathrm{m/s}$ and $\rho_0 = 1.2\,\mathrm{kg/m^3}$, respectively. Hence, the expected eigenfrequencies corresponding to the one-dimensional duct in the no-flow case are $f = 0\,\mathrm{Hz}$, $50\,\mathrm{Hz}$, $100\,\mathrm{Hz}$, $150\,\mathrm{Hz}$, and so on (cf. [32]). The corresponding circular frequencies are $\omega_k = 100\pi k\,\mathrm{Hz}$, with $k = 0, 1, 2, \ldots$

To analyze the appearance of spurious eigenvalues more closely, multiple test scenarios have been developed. For this, the Mach number is increased in three steps. The cases of $Ma = 0$, $Ma = 0.1$, $Ma = 0.5$, and $Ma = 0.9$ are considered. Within each step, the computation of the eigenvalue problem is carried out on two different meshes for each element type depicted in Figure 1. Table I provides a brief survey of the different meshes that have been used and the corresponding problem sizes, i.e., the number of degree of freedom (dof). These four meshes are depicted in Figure 5.

The first test case deals with the no-flow case, i.e., the case of $Ma = 0$. This investigation is chosen to confirm that Lagrangian elements are not suited to be applied to equation (9). The eigenvalues computed by using linear Lagrangian elements (cf. Figure 6a) are compared to

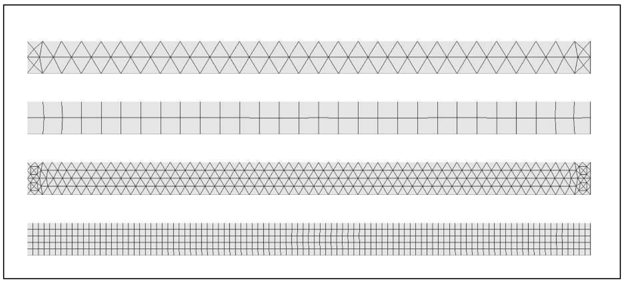

Figure 5. Duct meshed by triangular (a,c) and quadrilateral elements (b,d), coarse grid representing mesh case 1 (a,b), finer grids representing mesh case 2 (c,d).

Table I. Duct: Test cases which will be applied to each element depicted in Figure 1. The number of elements is denoted by n_{el} and "dof" represents the number of degrees of freedom.

	Mesh case 1		Mesh case 2	
	n_{el}	dof	n_{el}	dof
T3–3c	126	285	504	945
T4–3c	126	537	504	1953
T6–3c	126	725	504	2581
Q9–4c	58	680	500	5028

the solution which is achieved when using Mini elements (cf. Figure 6b). Both solutions appear to be purely real. Hardly any error is visible for the Mini elements for which the eigenvalues are equidistantly distributed along the real axis. However, the eigenvalues which are found by using Lagrangian elements seem to be randomly distributed along the real axis. Actually, the correct eigenvalues are evaluated similar to the Mini elements but, additionally, a number of other modes, the so-called spurious modes, are computed. Such spurious modes pollute the solution of the typical boundary value problem as demonstrated by Treyssède et al. [13]. These spurious modes, which occur for the no-flow problem, do not vanish for a Mach number greater than zero. Therefore, Lagrangian elements are not further taken into account in this study.

In the second test case, a Mach number $Ma = 0.1$ is considered. The eigenvalue distribution of two different meshes of Taylor-Hood triangular elements (T6–3c) is shown in Figure 7. At first glance, both plots show the complex eigenvalues almost arbitrarily distributed in the complex plane. However, the regularly appearing dots along the real axis correspond to the eigenvalues which have a physical meaning. The eigenvalues of spurious modes are all complex. This behavior is clearly observed for both meshes. A qualitatively similar result is obtained for the other two types of elements, i.e., T4–3c and Q9–4c. In all cases, the spurious modes clearly show eigenvalues with non-zero imaginary part. It is assumed that this is the reason why they have not been observed in other studies solving the boundary value problems [13, 16, 10, 12].

As stated above, eigenvalues of the quadratic eigenvalue problem (cf. equation 10) occur either as real values or as conjugate complex pairs. Consequently, the distribution

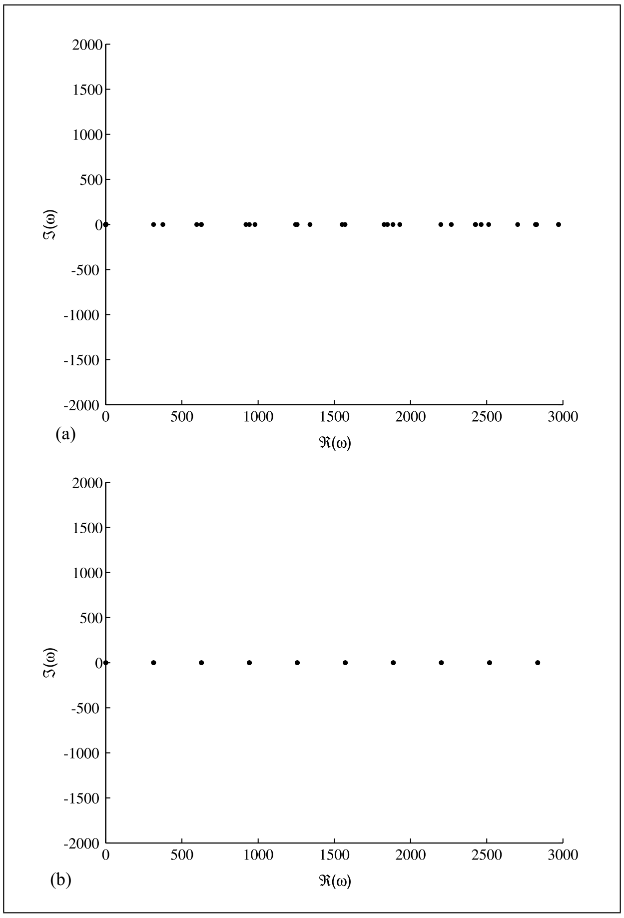

Figure 6. Duct: Test case 1: $Ma = 0$, mesh case 2: Comparison of eigenvalues ω_k for (a) Lagrangian elements and (b) Mini elements.

of eigenvalues in the complex plane should be symmetric with respect to the real axis. Results in Figure 7, and later on in Figures 9, 10, and 11b, show essentially symmetric distributions. However, at a close up they are not entirely symmetric, which is likely due to numerical approximation errors. At least, numerous computations confirm the location and uniqueness of eigenvalues along and close to the real axis and a generally correct distribution of the remaining ones.

It is not really practical, but, for the results of this example at least possible, to identify physical and spurious modes based on a visual impression of the eigenvectors. Figure 8 allows to compare two eigenmodes with adjacent frequencies around $f = 195\,\mathrm{Hz}$. In this case, the T6–3c elements are used on the finer mesh (i.e., mesh case 2). In the lower part of Figure 8a, the real and imaginary parts of the fourth mode of the numerical solution match well with the exact solutions (cf. equation 15). All outputs are scaled such that the greatest magnitude equals one. The spurious mode in Figure 8b is identified by its complex eigenfrequency of $f = 193.4 + 74.7i\,\mathrm{Hz}$, as shown. Moreover, it clearly contains high frequency waves which are not physical for a frequency of approximately 195 Hz. A rough estimate is always possible by using the equation $\lambda = c/f$. Of course this estimate holds for the no-flow case, but it

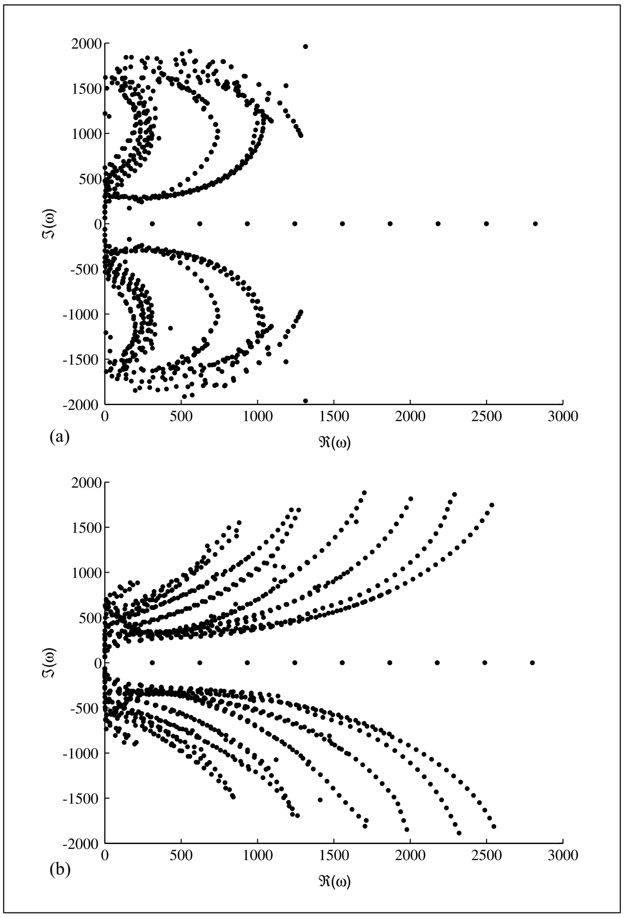

Figure 7. Duct: Test case 2: $Ma = 0.1$, Taylor-Hood elements T6–3c, eigenvalue distribution for two meshes (cf. Table I).

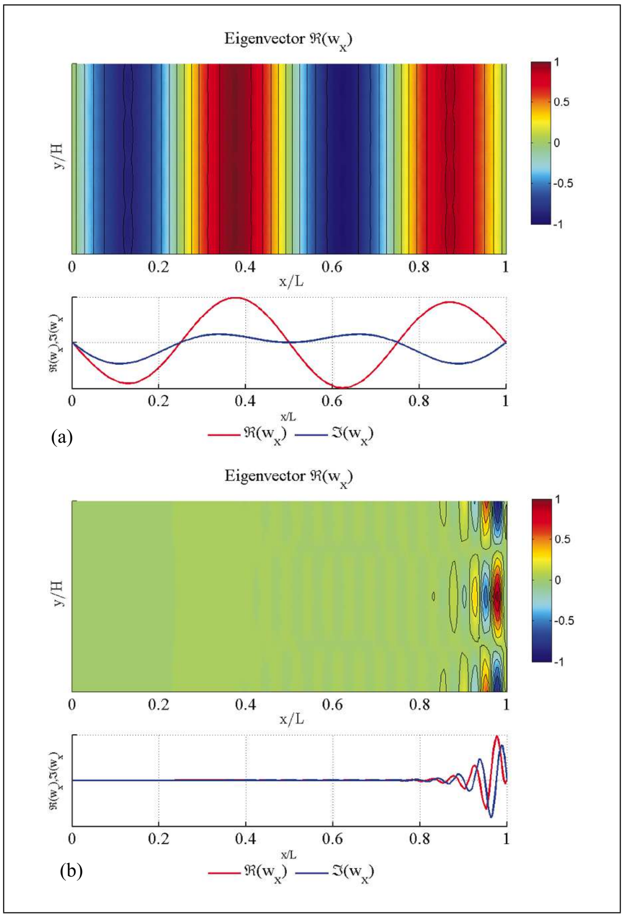

Figure 8. Duct: Test case 2: $Ma = 0.1$, Taylor-Hood elements T6–3c: Eigenvectors for w_x of a physical (a, $f = 198$ Hz) and a spurious (b, $f = (193.4 + 74.7i)$ Hz) mode close to 195 Hz. The lower subfigures show plots along the line of symmetry of the upper parts, i.e., along $y = H/2$.

is easily applicable for low Mach numbers as well. Based on the experience of the vorticity modes occurring for the solution of the Linearized Euler Equations (LEE) and as predicted by Brazier [19], it might be assumed that this could be a vorticity mode. However, it has been impossible to track this mode on different meshes and there has not been any indication of this mode being divergence free, and hence being a pure rotational mode.

Greater Mach numbers are studied in a third test case. Figures 9, 10, and 11b show the eigenvalue distributions for the Mini elements (T4–3c), triangular (T6–3c), and quadrilateral (Q9–4c) Taylor-Hood elements. These results are found for the mesh case 2, i.e., for the finer mesh.

The eigenvalue distribution of the solution using Mini elements confirms the observations of Gabard *et al.* [16]. Therein, the authors stated that the Mini elements perform stable up to a Mach number of 0.5. Beyond this, the solution may become unstable. This is clearly confirmed in Figure 9b. While the eigenvalues on the real axis are still evenly distributed in Figure 9a numerous additional and unwanted eigenvalues are observed in Figure 9b. These additional real eigenvalues of Mini elements are clearly related to spurious modes. (They disappear when using Taylor–Hood elements.) The ratio between length and width of the duct is 17, so that transverse modes cannot occur below $\omega = 5$kHz [35]. As expected, these transverse modes are not observed. There is no doubt that Mini elements are not suited for solution of the boundary value problem for Mach numbers approaching 1. However, this limit is not clarified in this work.

The situation is different for both variants of Taylor-Hood elements. Both, triangular (cf. Figure 10) and quadrilateral (cf. Figure 11b) elements, clearly distinguish eigenvalues on the real axis from the other ones. Again, eigenvalues on the real axis account for the physically relevant ones whereas complex eigenvalues are associated with spurious modes. For Mach numbers of 0.9, the spacing between the eigenvalues decreases dramatically. While the fourth non-zero eigenfrequency of the no-flow case is found at 200 Hz, and thus its circular frequency ω lies beyond 1200 Hz, for a Mach number of 0.9, 20 eigenfrequencies with circular frequencies below 1200 Hz (cf. equation 14) are expected. In the lower part of Figure 10b, 18 dots up to a circular frequency of 1200 Hz are counted, whereas, in that of Figure 11b, the actual number of 20 dots is identified. The increasing number of modes within a particular frequency range leads to significantly decreasing frequencies for which the mesh can be used.

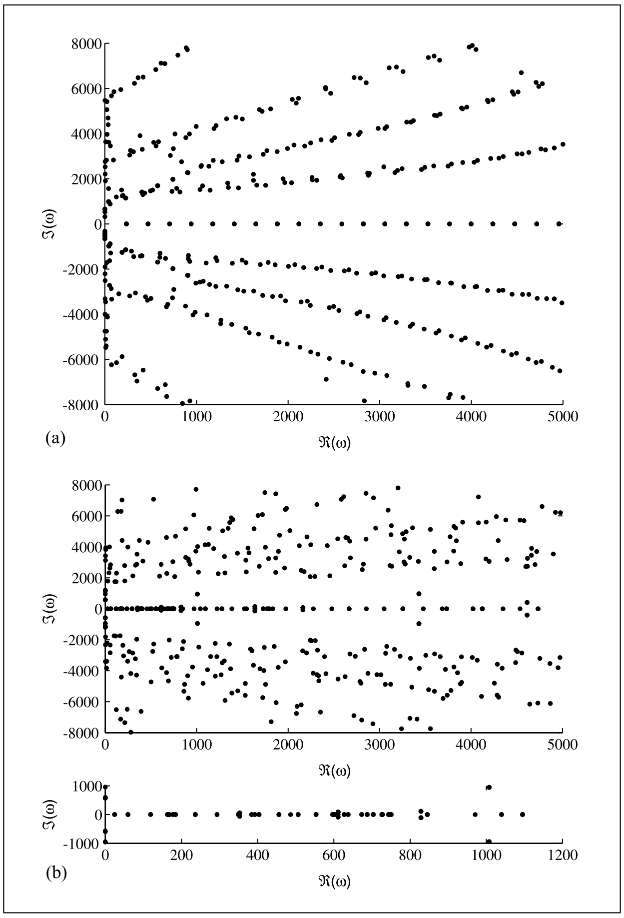

Figure 9. Duct: Test case 3: Mini elements T4–3c, mesh case 2, eigenvalue distribution for two Mach numbers. (a) $Ma = 0.5$, (b) $Ma = 0.9$.

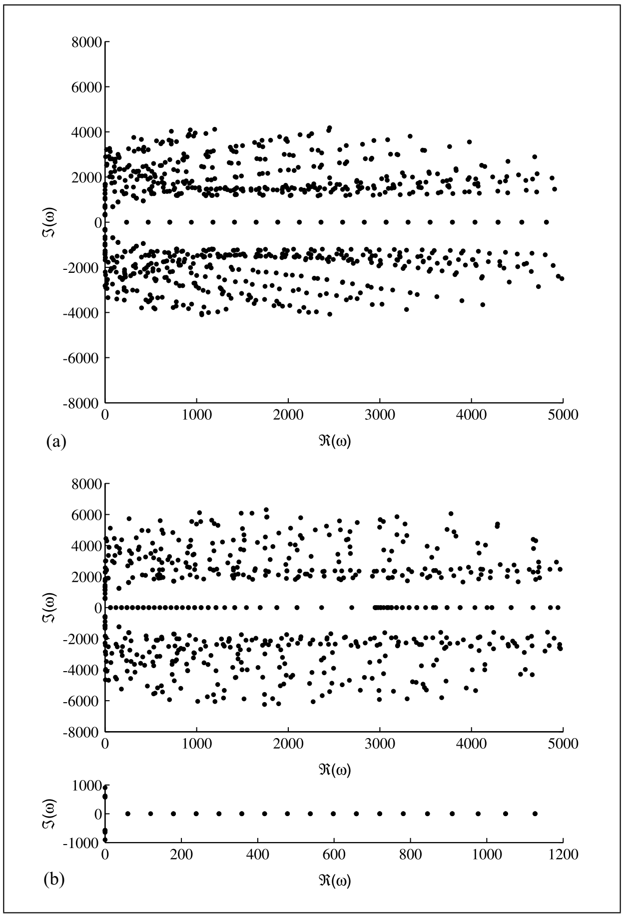

Figure 10. Duct: Test case 3: Taylor-Hood elements T6–3c, mesh case 2, eigenvalue distribution for two Mach numbers. (a) $Ma = 0.5$, (b) $Ma = 0.9$.

Many applications require determination of the lowest eigenvalues. Therefore, it is important to know up to which frequency the finite elements give accurate results. To achieve this, the relative error is defined as

$$\mathrm{e}^{\mathrm{rel}} = \left| \frac{\omega^{\mathrm{num}} - \omega^{\mathrm{ex}}}{\omega^{\mathrm{ex}}} \right|, \tag{16}$$

where ω^{num} represents the numerical solution and ω^{ex} the analytical solution of the one-dimensional problem.

Assuming the rule of thumb $kh < 1$ with wave number $k = \omega/c$ and element size h (cf. [36, 35]), it is expected for the finer meshes (i.e., mesh case 2) to allow more than 9.5 waves along the duct ($f < 950$ Hz in the no-flow case) for the triangles and almost 16 ($f < 1590$ Hz in the no-flow case) for the quadrilaterals. Tables II, III, and IV survey the maximum eigenfrequencies for which the numerical solution remains below a certain error for the finite elements that are considered. The right-hand parts of these tables contain the maximum number of waves in the duct to remain below this certain error in the eigenfrequency. Note that this happens because the wavelength shortens for increasing Mach number.

Table II. Duct: Mesh case 2, Mini elements T4–3c: Limitations of element type.

	Maximum eigenfrequency f in Hz for		
Ma	$\mathrm{e}^{\mathrm{rel}} \leq 0.01\%$	$\mathrm{e}^{\mathrm{rel}} \leq 0.1\%$	$\mathrm{e}^{\mathrm{rel}} \leq 1\%$
0	50	250	850
0.1	198	396	891
0.5	75	262	562
0.9	0	10	19
	Maximum number of waves for		
Ma	$\mathrm{e}^{\mathrm{rel}} \leq 0.01\%$	$\mathrm{e}^{\mathrm{rel}} \leq 0.1\%$	$\mathrm{e}^{\mathrm{rel}} \leq 1\%$
0	0.5	2.5	8.5
0.1	2	4.0	9.0
0.5	1	3.5	7.5
0.9	0	0.5	1.0

3.4. Duct with admittance boundary conditions at end caps

Eigenvalues of the system with admittance boundary conditions at end caps can be analytically found when the condition of equation (7) is used. Obviously, this condition is not valid for a physically realistic model since it neglects

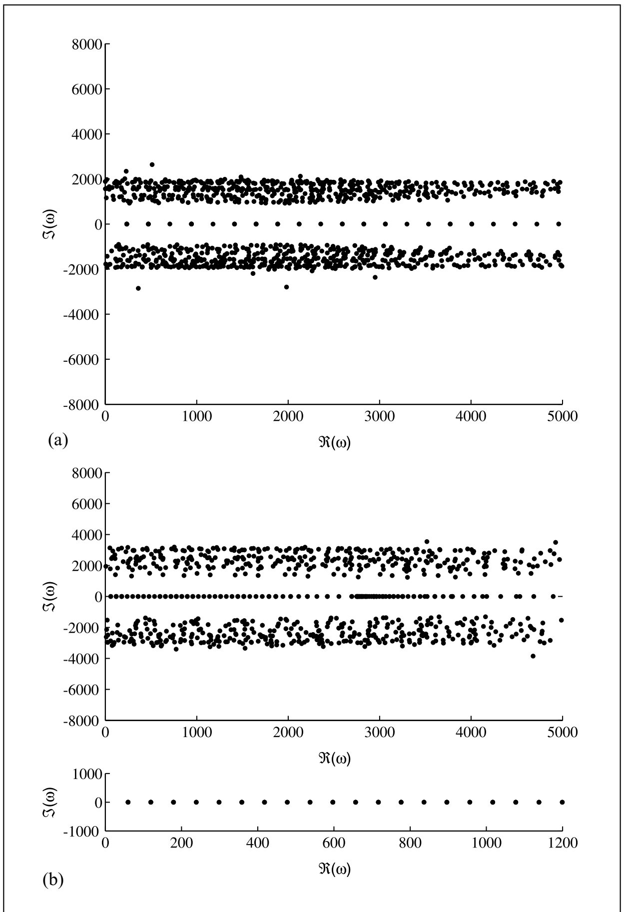

Figure 11. Duct: Test case 3: Taylor-Hood elements Q9–4c, mesh case 2, eigenvalue distribution for two Mach numbers. (a) Ma = 0.5, (b) Ma = 0.9.

Table III. Duct: Mesh case 2, Taylor-Hood elements T6-3c: Limitations of element type.

	Maximum eigenfrequency f in Hz for		
Ma	$e^{rel} \leq 0.01\%$	$e^{rel} \leq 0.1\%$	$e^{rel} \leq 1\%$
0	250	550	950
0.1	346	594	940
0.5	262	412	638
0.9	48	86	124
	Maximum number of waves for		
Ma	$e^{rel} \leq 0.01\%$	$e^{rel} \leq 0.1\%$	$e^{rel} \leq 1\%$
0	2.5	5.5	9.5
0.1	3.5	6.0	9.5
0.5	3.5	5.5	8.5
0.9	2.5	4.5	6.5

the fact that the end caps are inlet and outlet of the duct. The solution would be very similar to the one in [32]. This means that, for the formulation used in this paper, the complex eigenvalues have a small but virtually constant imaginary part. Hardly any difference in comparison to the non-dissipative system will be observed. For this reason, the example of the duct with admittance boundary conditions

Table IV. Duct: Mesh case 2, Taylor-Hood elements Q9–4c: Limitations of element type.

	Maximum eigenfrequency f in Hz for		
Ma	$e^{rel} \leq 0.01\%$	$e^{rel} \leq 0.1\%$	$e^{rel} \leq 1\%$
0	450	850	950
0.1	594	891	940
0.5	412	675	825
0.9	76	133	218
	Maximum number of waves for		
Ma	$e^{rel} \leq 0.01\%$	$e^{rel} \leq 0.1\%$	$e^{rel} \leq 1\%$
0	4.5	8.5	9.5
0.1	6.0	9.0	9.5
0.5	5.5	9.0	11.0
0.9	4.0	7.0	11.5

at end caps will not be discussed in more detail in this work.

4. Computational example II - Shear flow in annulus with rigid boundary

4.1. Model description

In the second computational example, an annulus with rigid boundary conditions and shear flow is investigated. As shown in Figure 12, the domain is bounded by the inner and the outer circle of radius r_1 and r_2, respectively. These radii are set to 0.75 and 1.0 m, respectively. Different from the other examples of this paper, the material data are set to unit values to make it easier to distinguish different orders of magnitude between displacement $\boldsymbol{w}$ and sound pressure p of the modes. This is useful to distinguish acoustic modes, vorticity modes and spurious modes. According to Brazier [19], vorticity modes are pure rotational modes and hence divergence free. Consequently, the sound pressure vanishes for these modes. In its turn, acoustic modes are rotation free and result in components of both, the displacement and the sound pressure, of the same order of magnitude, which also can be followed from equation (8).

A shear flow profile is used as shown in Figure 12. The flow velocity in terms of the radius r is formulated as

$$v_\varphi = \frac{c_0}{2}\left\{\frac{2}{r_2 - r_1}\left[r - \frac{r_2 + r_1}{2}\right]\right\}. \tag{17}$$

Notice that the velocity of the shear flow profile was chosen as simple as possible (linear with respect to r). Hence, the Mach number in the circumferential direction at the inner and the outer radii is −0.5 and 0.5, respectively.

Six different meshes of Taylor-Hood elements (T6-3c and Q9-4c) have been used for this example. Details about them are given in Table V. For each mesh, the 300 eigenvalues closest to the segment with end points $(0, 0i)$ and $(1, 0i)$ are evaluated.

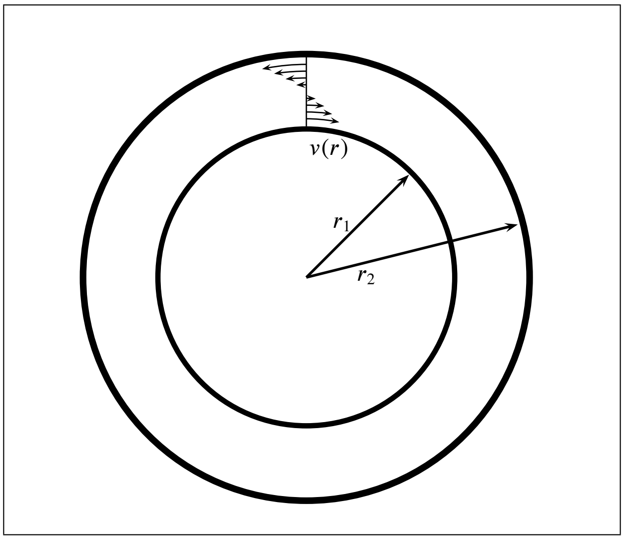

Figure 12. Annulus: Domain and flow profile of the two-dimensional problem.

Table V. Shear flow in annulus: Mesh details of different test cases.

case	element type	n_{el}	dof
mesh 1	T6-3c	298	1551
mesh 2	Q9-4c	149	1601
mesh 3	Q9-4c	268	2792
mesh 4	T6-3c	786	3917
mesh 5	T6-3c	2280	10960
mesh 6	T6-3c	8912	41484

4.2. Eigenvalues and acoustic modes in the vicinity of the origin

Figure 13 shows eigenvalue distributions. Note that different scales are used for different meshes. The eigenvalue distribution looks similar to the mean flow example of the duct. Actually, with respect to the numerical behavior, hardly any difference is observed between the mean flow example and the shear flow example.

The location of acoustic modes is easily identified on the real axis. According to the eigenvalues which are given in Table VI, it is obvious that they are converging very well and even for the coarsest meshes, the error is below 0.1%. In some of the cases, even higher order acoustic modes have been computed but they are not considered in this example. Figure 14 shows these mode shapes as radial displacement w_r, circumferential displacement w_φ and sound pressure p. Similar to the solution of the Helmholtz equation, two modes are evaluated. Both show a single circumferential wave. The difference to the Helmholtz equation consists in the mode splitting as they occur at different eigenvalues which is due to the flow. When tracking these modes, their shape remains the same from the coarsest to the finest mesh. Hence, the mode shapes are converging well in addition to the eigenvalues.

4.3. Vorticity modes and spurious modes

In addition to acoustic modes, Brazier [19] predicted the existence of vorticity modes. Based on his solution, the smallest eigenvalues of the vorticity modes should be of lower magnitude than the eigenvalues of the acoustic modes, as long as $Ma \leq 0.5$, which is the case in this example. Since the prediction has been such that these vorticity modes are divergence free, they should be identified by a sound pressure which is small compared to the displacement. Taking this into account, it was tried to identify and track these rotational modes. Pure rotational modes have been only identified as modes with imaginary eigenvalues. Eigenvalues of the first three rotational modes are collected for the six meshes in Table VII.

Figures 15 and 16 show the mode shapes of the first and the second modes respectively, which are associated with the lowest imaginary eigenvalues. Although (nearly) fulfilling the condition to be divergence free, the rotational modes do not converge to a specified shape. Nevertheless, a certain physically reasonable and repeated structure of the modes is observed. The first modes, depicted in Figure 15 represent a wide rotational displacement within the duct for the coarsest mesh. For the finer meshes, the structure of the mode shape remains similar but the width of the rotational displacement becomes much smaller. Note that mode shapes can be arbitrarily scaled. Furthermore, the eigenvalues associated with these modes are clearly depending on the mesh size as shown in Table VII. The missing convergence of eigenvalues indicates that these modes are spurious modes.

Investigation of other modes associated with the smallest eigenvalues in the first quadrant shows that there are numerous other mode shapes for which the pressure component is one order of magnitude smaller than the displacement. These mode shapes are close to rotational modes, although not that clearly exposed as those which have been discussed above. They can be categorized in terms of the number of pressure waves within the annulus. These modes are somewhat similar to the acoustic modes, since they present one, two, three, and even more pressure waves in the annulus. However, the displacement component does not clearly correspond to these pressure waves.

The modes which expose a single circumferential pressure wave are tracked within the rectangle of the complex plane ($[0, 1] \times [0, i]$). Numerous of these modes could be found there. In general, it can be stated that the finer the mesh, the more of these modes are found in the rectangle. However, neither eigenvalues nor the displacement component of the mode shapes converges. The eigenvalues of these modes within the specified rectangle are assembled in Table VIII. Figure 17 shows two modes which look similar to the first acoustic modes when considering the sound pressure component only. These are the modes 1 and 2 for mesh 6 in Table VIII. Again, missing convergence of eigenvalues and mode shapes indicates that these are spurious modes.

Similar to the observations of spurious modes with one pressure wave in the annulus can be reported for modes

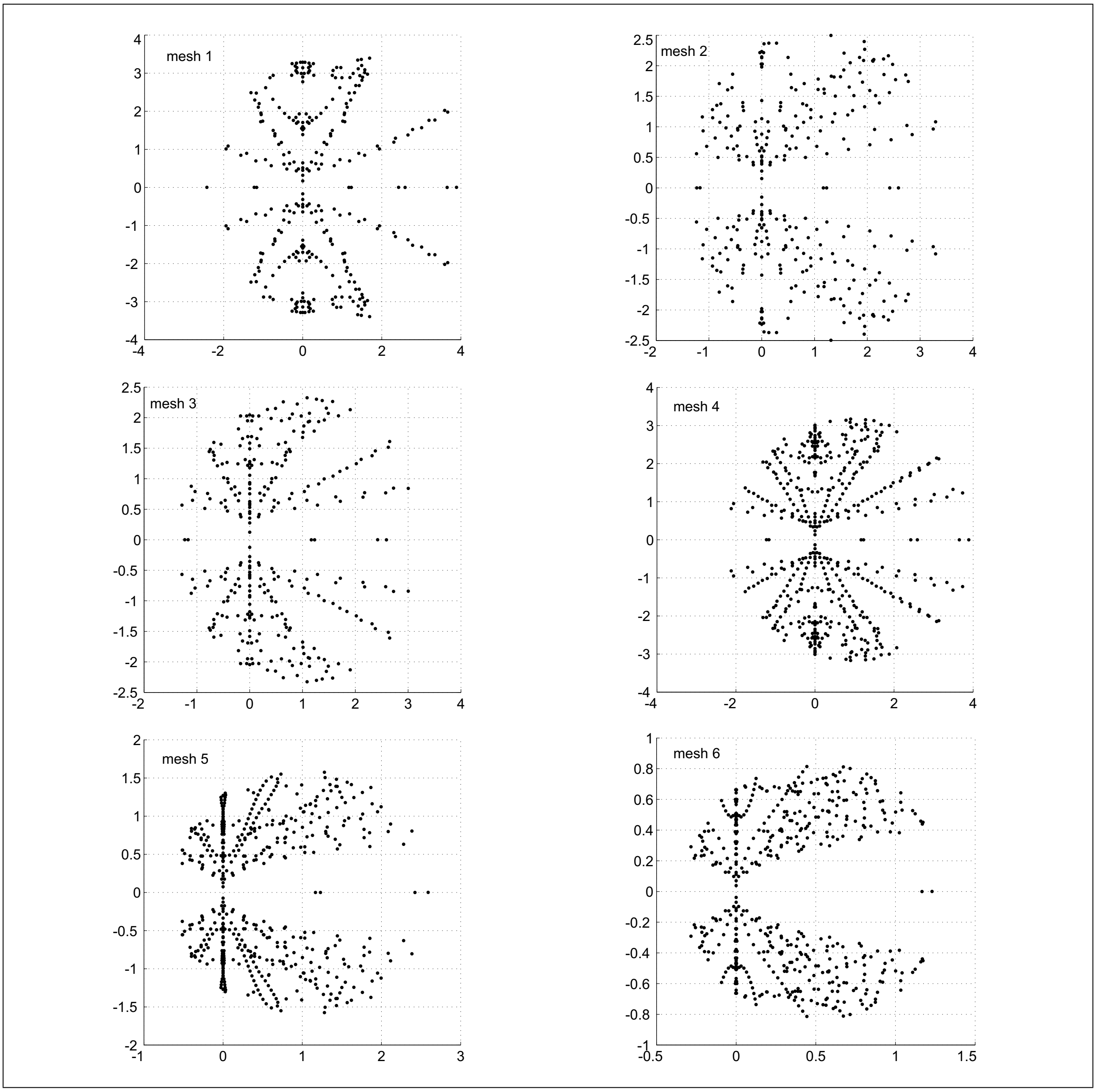

Figure 13. Shear flow in annulus: Distribution of eigenvalues in complex plane in the vicinity of the segment of endpoints $(0, 0i)$ and $(1, 0i)$ for different meshes.

Table VI. Shear flow in annulus: Eigenvalues of first two acoustic modes for six different meshes.

mesh	1	2	3	4	5	6
acoustic mode 1	1.1670	1.1672	1.1667	1.1667	1.1667	1.1667
acoustic mode 2	1.2292	1.2298	1.2295	1.2293	1.2294	1.2293

Table VII. Shear flow in annulus: Eigenvalues of first three rotational modes for six different meshes.

mesh	1	2	3	4	5	6
rotational mode 1	$0.1609i$	$0.1522i$	$0.1245i$	$0.1322i$	$0.0750i$	$0.0387i$
rotational mode 2	$0.3191i$	$0.2749i$	not found	$0.2332i$	$0.1273i$	$0.0702i$
rotational mode 3	$0.4494i$	not found	not found	$0.3493i$	$0.2158i$	$0.1118i$

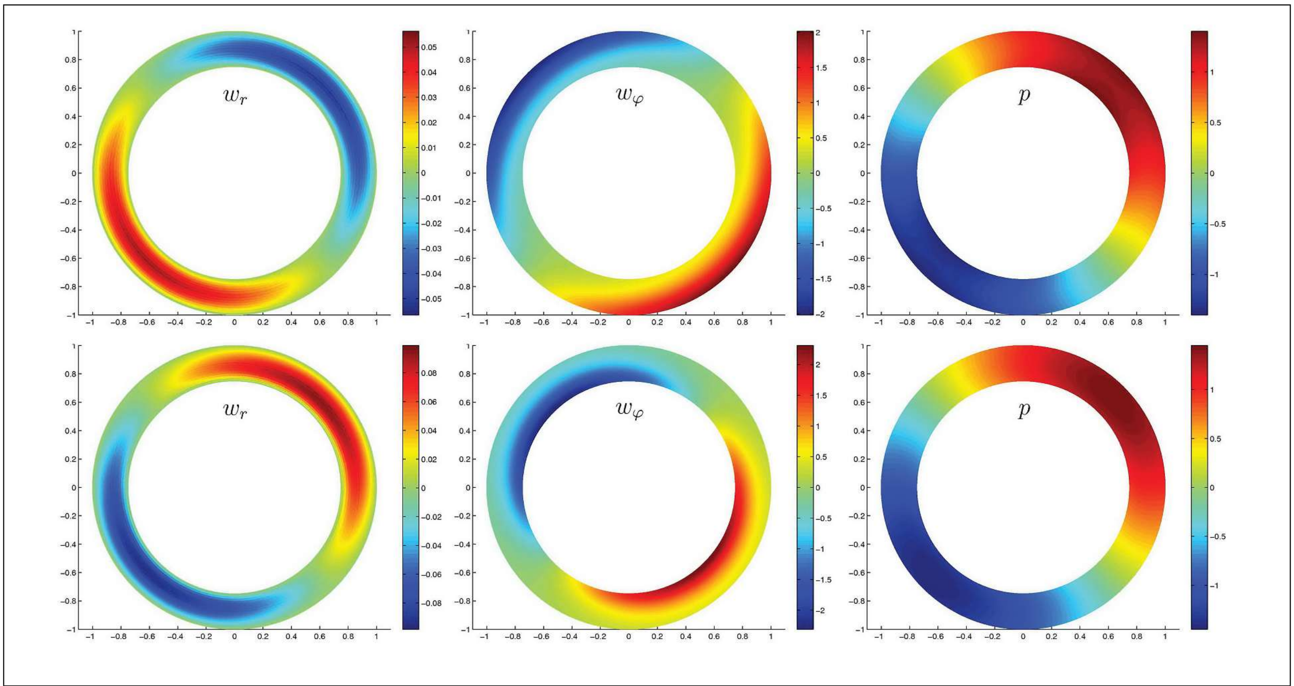

Figure 14. Shear flow in annulus: mesh 6: acoustic modes shapes, eigenvalues 1.1667 (top) and 1.2293 (bottom).

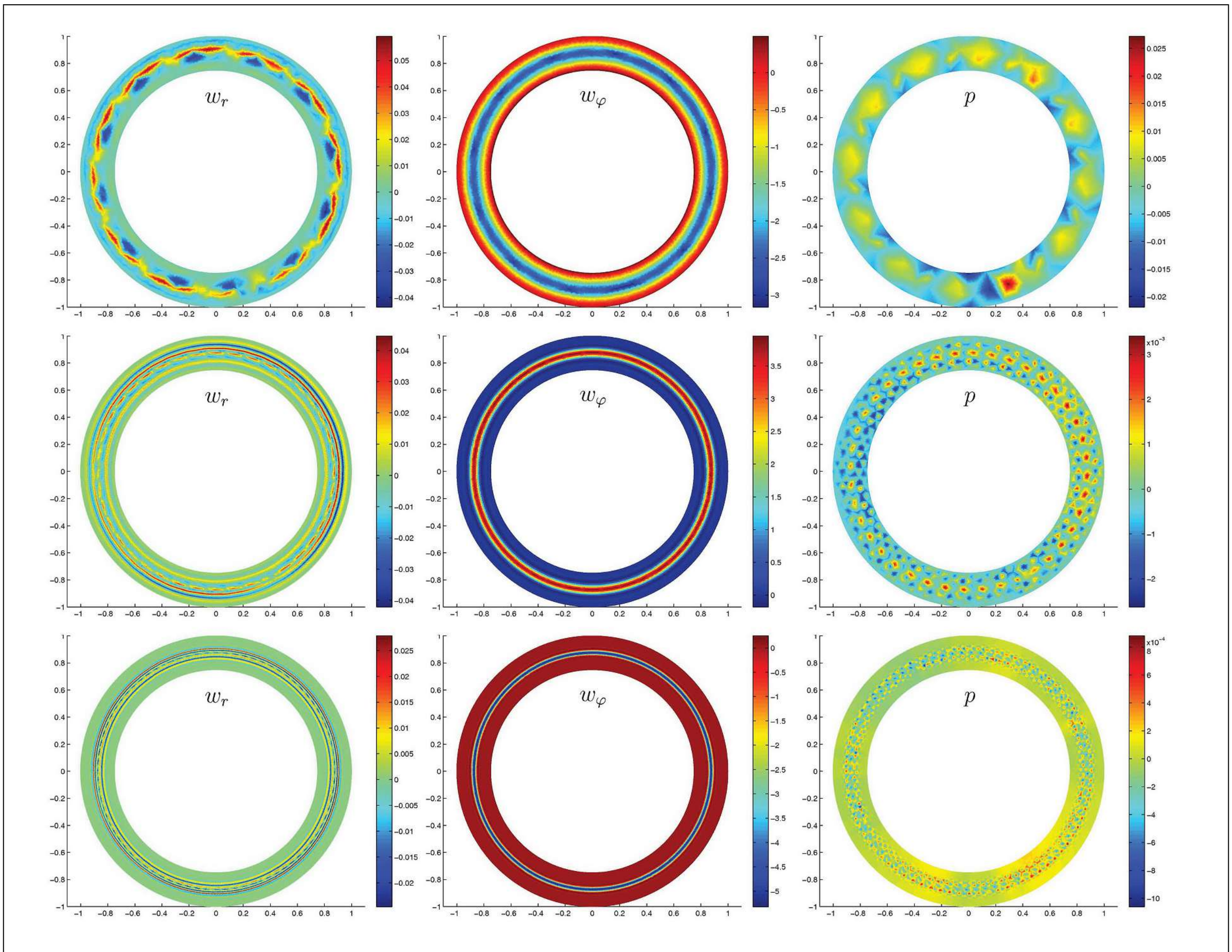

Figure 15. Shear flow in annulus: meshes 1 (top), 5 (center), 6 (bottom): development of first divergence free modes shapes on different meshes.

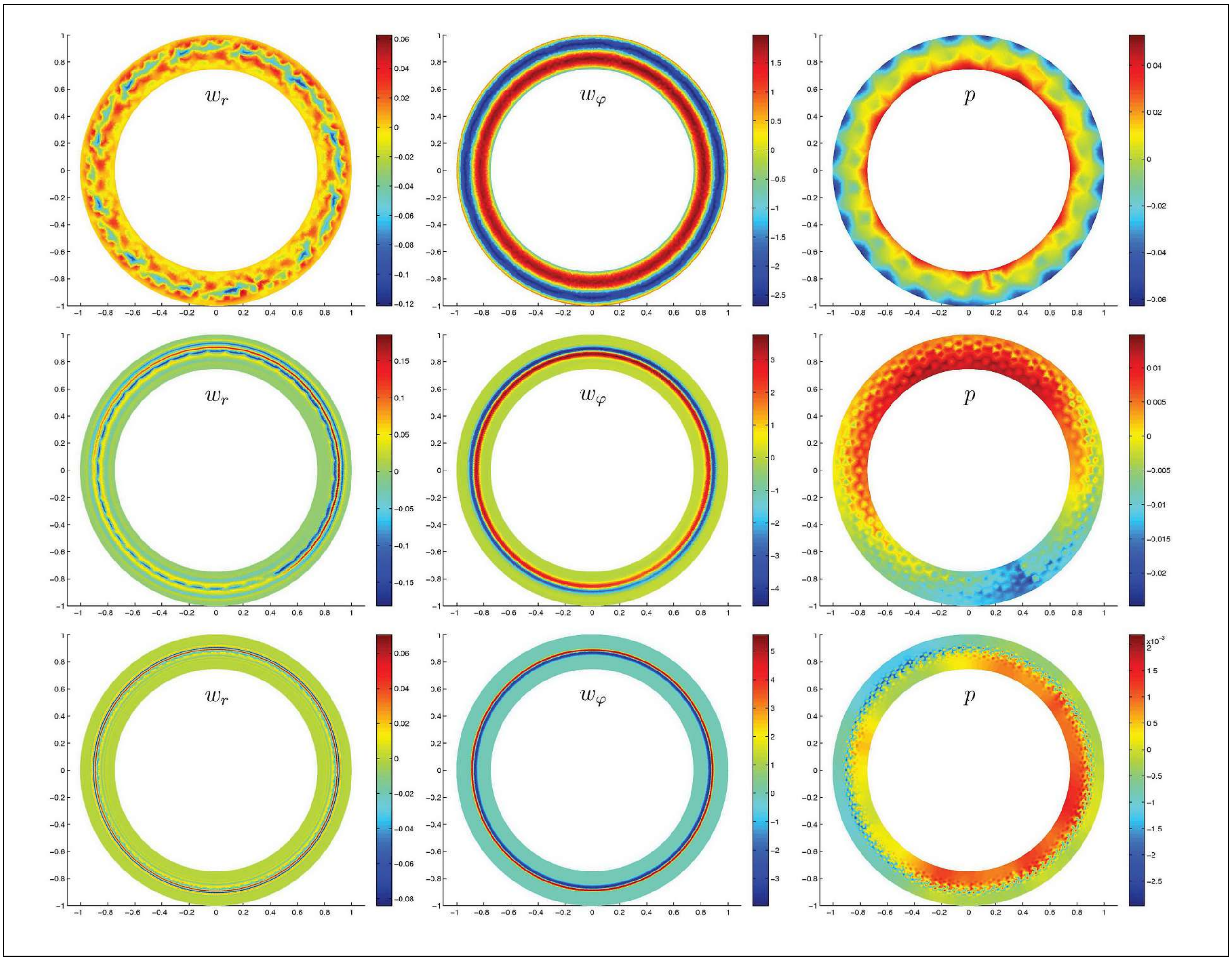

Figure 16. Shear flow in annulus: meshes 1 (top), 5 (center), 6 (bottom): development of second divergence free modes shapes on different meshes.

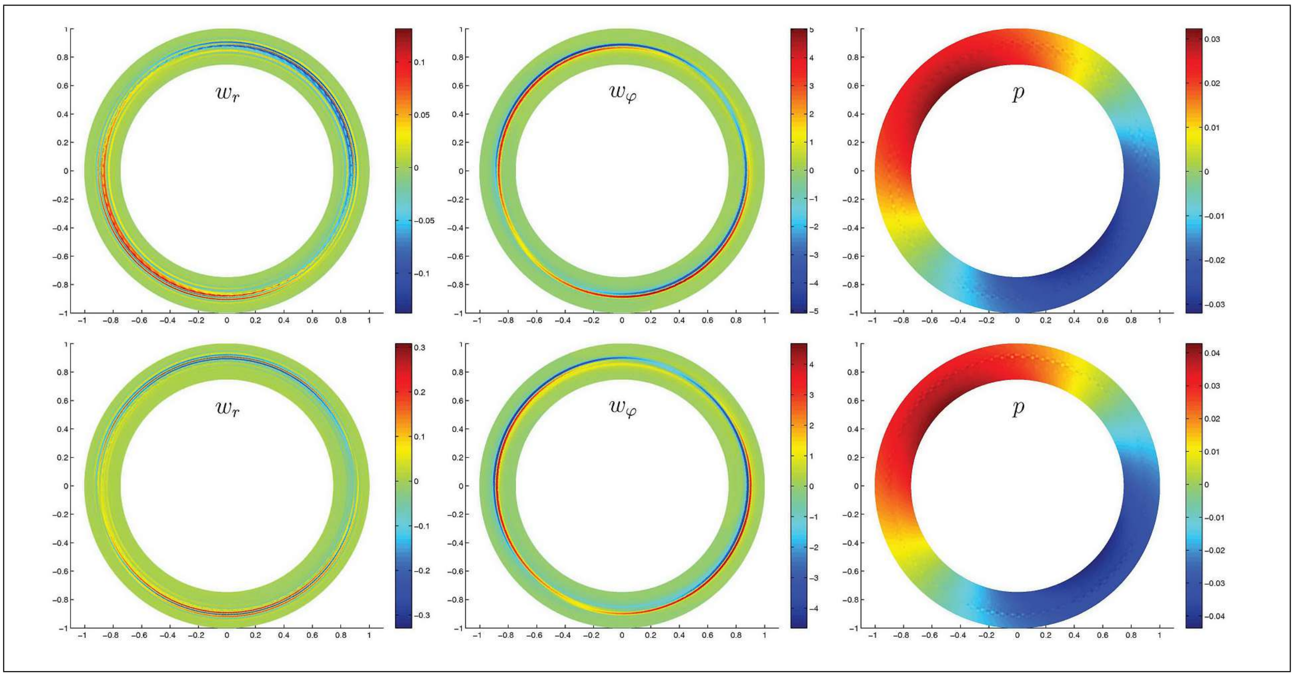

Figure 17. Shear flow in annulus: mesh 6: two spurious modes exposing a single pressure wave in the annulus. Eigenvalues given in Table VIII for modes 1 (top) and 2 of mesh 6.

Table VIII. Shear flow in annulus: Eigenvalues of rotational modes with one circumferential pressure wave in specified rectangle for six different meshes.

mesh	1	2	3	4	5	6
mode 1	$0.16+0.43i$	$0.16+0.38i$	$0.17+0.38i$	$0.05+0.34i$	$0.02+0.18i$	$0.01+0.10i$
mode 2	$0.11+0.48i$	$0.43+0.46i$	$0.18+0.42i$	$0.12+0.36i$	$0.13+0.27i$	$0.07+0.13i$
mode 3	$0.40+0.48i$		$0.42+0.47i$	$0.31+0.49i$	$0.11+0.25i$	$0.05+0.13i$
mode 4	$0.47+0.61i$		$0.54+0.61i$	$0.39+0.52i$	$0.26+0.32i$	$0.13+0.18i$
mode 5				$0.30+0.49i$	$0.30+0.40i$	$0.12+0.19i$
mode 6				$0.57+0.68i$	$0.42+0.43i$	$0.20+0.24i$
mode 7					$0.52+0.55i$	$0.21+0.27i$
					more	more

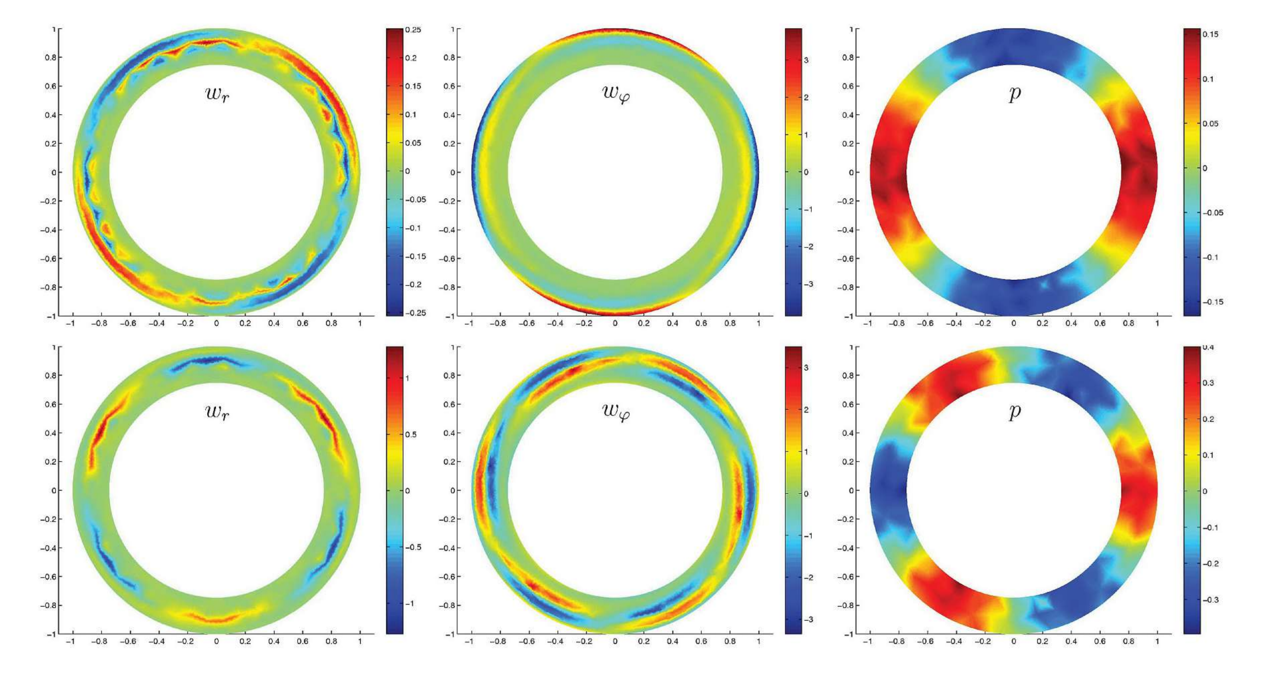

Figure 18. Shear flow in annulus: mesh 1: spurious modes exposing two (top) and three pressure waves in the annulus.

with more than one pressure wave in the annulus. Examples of two of these modes are depicted in Figure 18. The physics of pressure waves in circumferential direction is not supported by the displacement plots. Moreover, eigenvalues and eigenvectors of these modes do not converge to specific values and shapes, respectively.

To attain a better understanding of mode shapes presented as contour plots in Figures 14-18, Figure 19 shows vector plots of the displacement fields corresponding to:

- top left of Figure 19: first acoustic mode (top of Figure 14);
- top right from Figure 19: first spurious mode (top of Figure 17);
- bottom left of Figure 19: first divergence free mode on mesh 6 (bottom of Figure 15);
- bottom right of Figure 19: second divergence free mode on mesh 6 (bottom from Figure 16).

Figure 19 exhibits the same information as the subfigures mentioned. However, presentation of results can be helpful to better understand the vectorial behavior of the displacement $\boldsymbol{w}$ within the eigenvectors.

Finally, it has not been possible to find vorticity modes, although other regions of the complex plane have been also investigated. However, this does not mean that there have not been any of them. This investigation has shown just that they do not occur among the modes belonging to the smallest eigenvalues. If these vorticity modes really exist for this example, it is likely that they occur for larger eigenvalues. An extended investigation of this phenomenon, however, is beyond the scope of this article.

5. Computational example III - Annulus with absorbing boundary

The third computational example considers the annulus again. This time, the outer boundary is an absorbing boundary. However, the example does not aim at a non-reflecting boundary condition. The boundary condition is chosen such that the distribution of eigenvalues of physical and spurious modes is comparable to the situation of a discretized exterior problem as in [20, 37, 38, 39, 40, 41, 42]. In these cases, some of the physical modes exhibit com-

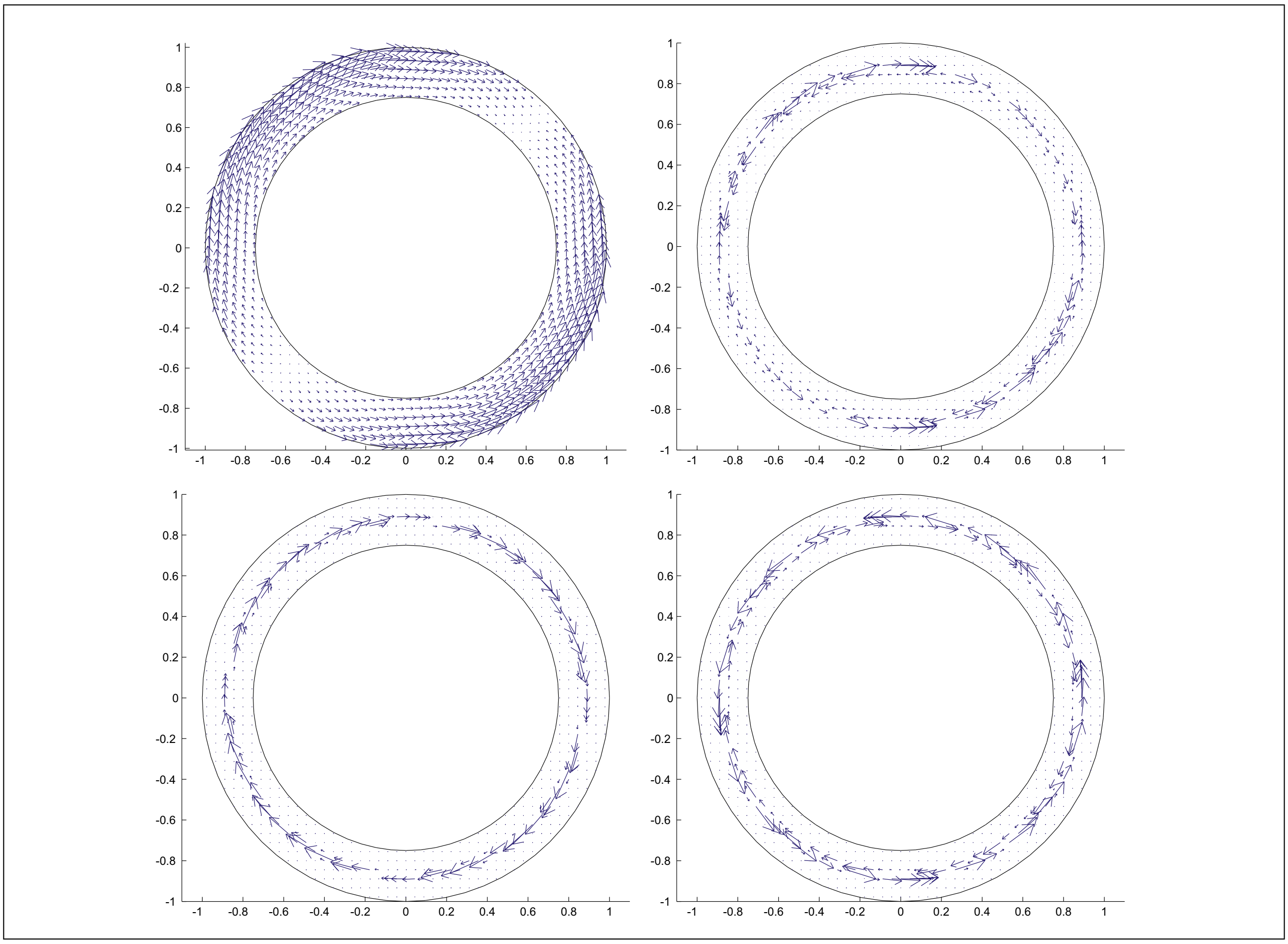

Figure 19. Shear flow in annulus: mesh 6: Vector plots of the displacement $\boldsymbol{w}$ for first acoustic mode (top left), the first two divergence free modes shapes (bottom left and bottom right, respectively) and first spurious mode as shown in Figure 17 (top right).

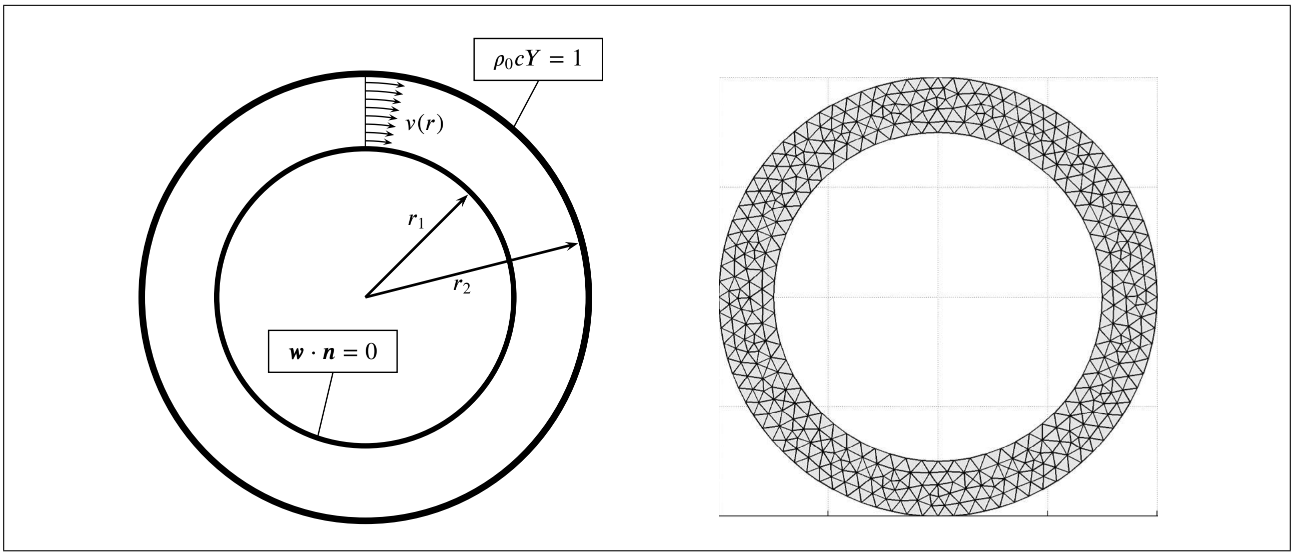

Figure 20. Annulus: Domain and mesh of the two-dimensional problem.

plex eigenvalues with large imaginary part of similar magnitude as the real part. It is expected that these eigenvalues mix up with the eigenvalues of spurious modes. Therefore, separation of physical and spurious modes will be much more difficult than in the previous examples.

5.1. Model description

An annulus domain accounts for the third computational example. As in the first one, the material data of air are used, i.e., $c_0 = 340\,\mathrm{m/s}$ and $\rho_0 = 1.2\,\mathrm{kg/m^3}$. The domain is bounded by an inner and an outer circle of radius r_1 and

r_2, respectively (cf. Figure 20). The radii of the inner and the outer circle are set to be 0.75 and 1.0 m, respectively.

Further, a steady ambient flow in the circumferential direction is assumed. The velocity profile is assumed to be linear in terms of the radius as

$$\boldsymbol{v} = \begin{bmatrix} v_r \\ v_\varphi \end{bmatrix} = \begin{bmatrix} 0 \\ r\omega_\varphi \end{bmatrix}, \tag{18}$$

with ω_φ being the (constant) angular velocity of the flow. It will be referred to the Mach number as the flow velocity at the outer boundary related to the speed of sound. Hence, $Ma = v_\varphi(r_2)/c_0$. For the inner boundary, the boundary condition is assumed as in equation (6):

$$w_r(r_1) = 0. \tag{19}$$

Again, this boundary condition represents a rigid (i.e., fully reflecting) wall. The condition at the outer boundary represents absorption. With respect to equation (7), this means

$$\rho_0 c_0 Y = \tilde{Y} = 1 \tag{20}$$

and, thus,

$$-\mathrm{i}\omega\rho_0 c_0 \boldsymbol{w}_r(r_2) = p(r_2). \tag{21}$$

Different from the tests in the previous sections, only triangular Taylor-Hood elements (T6–3c) are used for the analysis of the annulus. This restriction is used since Mini elements have shown limitations in the previous example. Quadrilateral Taylor–Hood elements (Q9–4c) are not reported because they behave similarly to the triangular ones.

The finite element model of the annulus consists of 786 triangular T6–3c elements (cf. Figure 20, right). This results in 469 nodes and 3917 degrees of freedom. Note that a cubic eigenvalue problem results in three eigenvalues per degree of freedom. However, fewer eigenvalues are determined since the leading matrix and the frequency independent matrix $\boldsymbol{A}$ are both singular. The cubic eigenvalue problem is solved iteratively within the software COMSOL Multiphysics [24].

In order to obtain a reference eigenvalue distribution, the eigenvalue problem is solved for the no-flow case first, i.e., $Ma = 0$. Figure 21 shows the eigenvalues of lowest magnitude. Clearly, the spectrum is free of spurious modes as expected for the no-flow case (i.e., a mixed finite element solution of the Helmholtz equation). Some of the modes, in particular purely imaginary modes and modes in the region determined by $1900 < \Re(\omega) < 2800$ and $2400 < \Im(\omega) < 2600$ look like the basic modes of external problems, as identified in [38]. These are the monopole (eigenvalue $2769 - 2412$i), two dipoles ($2735 - 2431$i), two quadrupoles ($2595 - 2488$i) and two hexapoles ($1988 - 2581$i). Other modes look more like standing waves in the circumferential direction. Low order modes are missing, the first of these modes (eigenvalue $2593 - 983$i) shows five waves over the circumference. Subsequent modes with eigenvalues $3025 - 797i$ and

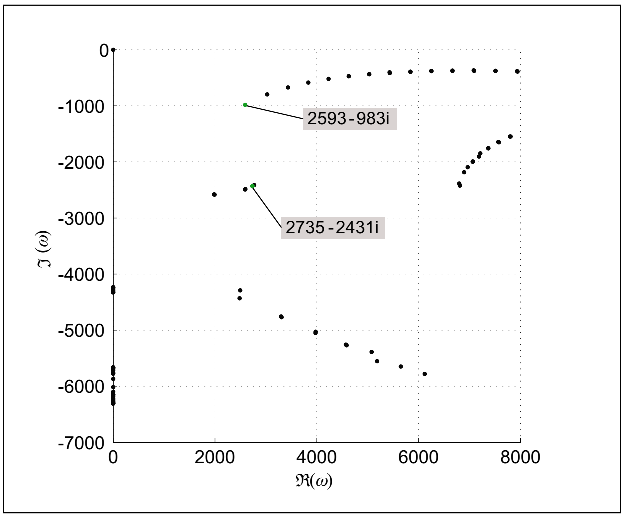

Figure 21. Eigenvalue distribution for $Ma = 0$.

$3434 - 673$i consist of six and seven waves, respectively. In comparison to [38], it is worth mentioning that real eigenvalues in this paper can be compared with imaginary eigenvalues in the former one. Recall that eigenvectors can be scaled arbitrarily. One dipole mode and the circumferential mode of five waves are depicted in Figure 22. These modes correspond to the green dots indicating their eigenvalues in the complex plane in Figure 21. Note that only the sound pressure component is shown in Figure 22.

Similar to the duct case, the Mach number is increased in three steps. Again, the cases of $Ma = 0.1$, $Ma = 0.5$, and $Ma = 0.9$ are considered. As in the previous examples, physical modes which have been found are pure acoustic modes. Furthermore, numerous spurious modes could be identified. Since the acoustic modes are well identified by their sound pressure component, the plots of radial and circumferential displacements are omitted.

For $Ma = 0.1$ (cf. Figure 23), the distribution of physical eigenvalues in the complex plane is polluted by spurious modes. However, it is still possible to make assumption on which modes might be physical. In particular, the right-hand part of the graph seems to be free of spurious solutions. Low order modes, however, must be sought among numerous false eigenvalues. As an example, Figure 23 shows the eigenvalues of two physical (green) and two spurious modes (red) which are located closely together. The mode shapes are depicted in Figure 24 for the physical and in Figure 25 for the spurious modes. A distinction between them is possible with respect to the acoustic wavelength. The modes in Figure 24 are identified by the wavelength λ which is close to $\lambda = c/f_i$ with frequency $f_i = \Re\{\omega_i/(2\pi)\}$ (where ω_i represents the eigenvalue) and the effective speed of sound given by $c = c_0 \pm v_0$. In this example, spurious modes are identified by shorter wavelengths as shown in Figure 25.

For $Ma = 0.5$ and $Ma = 0.9$ (cf. Figure 26), spurious solutions are spread all over the shown rectangle. A visual distinction between physical and spurious modes is almost impossible. In both subfigures, two physical and two spu-

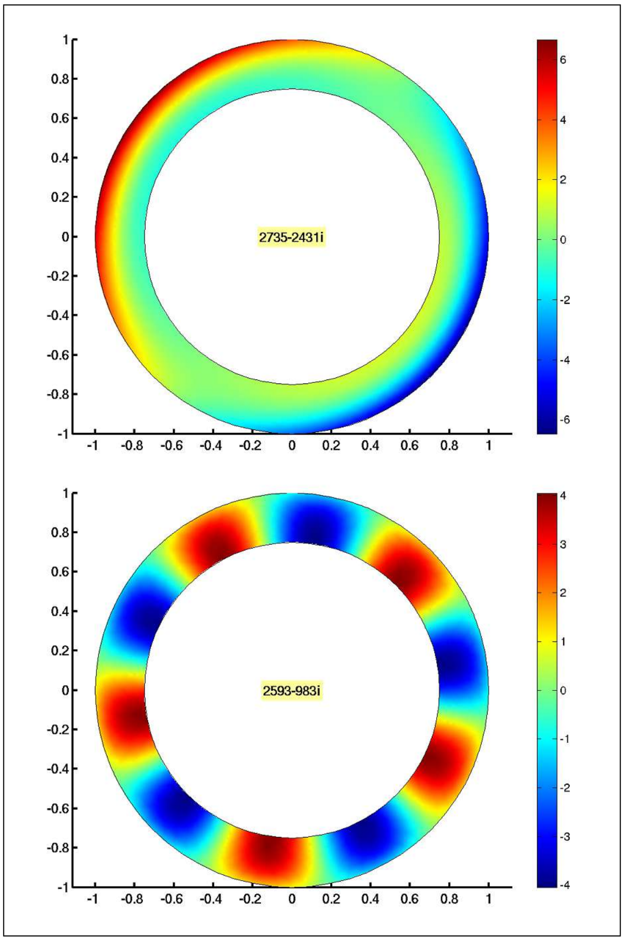

Figure 22. Two arbitrarily chosen eigenvectors (sound pressure component only) for the case $Ma = 0$, dipole mode (top) and mode with five circumferential waves (bottom); eigenvalue shown in the center of the annulus.

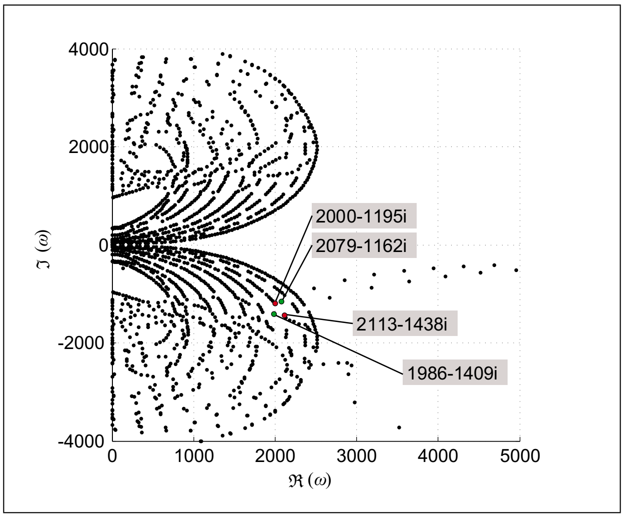

Figure 23. Eigenvalue distribution for $Ma = 0.1$.

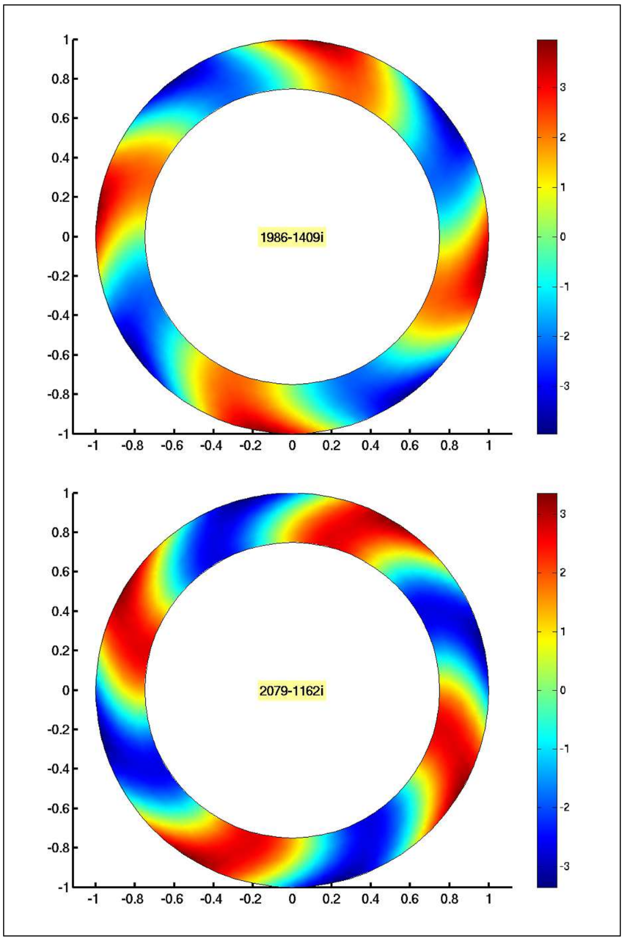

Figure 24. Sound pressure component of two physical modes for $Ma = 0.1$; eigenvalue shown in the center of the annulus.

rious solutions are marked in green and red, respectively. The corresponding physical modes are depicted in Figure 27 for $Ma = 0.5$ and in Figure 28 for $Ma = 0.9$. Identification of physical modes based on their wavelengths is still possible. For instance, Figure 28 (right) corresponds to a distorted dipole mode. The distortion results from the flow field. In addition to the physical modes, an investigation of the spurious ones which are marked in Figure 26 has shown a similar pressure distribution as in Figure 25. Finally, the authors find it worth mentioning that for $Ma = 0.9$ (cf. Figure 26, right), the eigenvalues closest to the real axis with $1200 < \Re(\omega) < 3000$ are all physical modes.

6. Conclusions

In this study, the acoustic eigenvalue problem in the presence of an ambient flow described by the Galbrun equation is analyzed numerically using a mixed finite element formulation. The results of eigenvalues and eigenvectors for a straight duct and for an annulus with an absorbing wall are discussed.

In the case of the energy conserving duct problem, the study basically confirms former results available in the literature. For Mach numbers up to 0.5, Mini elements seem to perform reliably, whereas, for higher flow velocities, real spurious eigenvalues occur. Taylor-Hood elements, both triangular and quadrilateral, seem to perform robustly even for a Mach number 0.9. However, except for

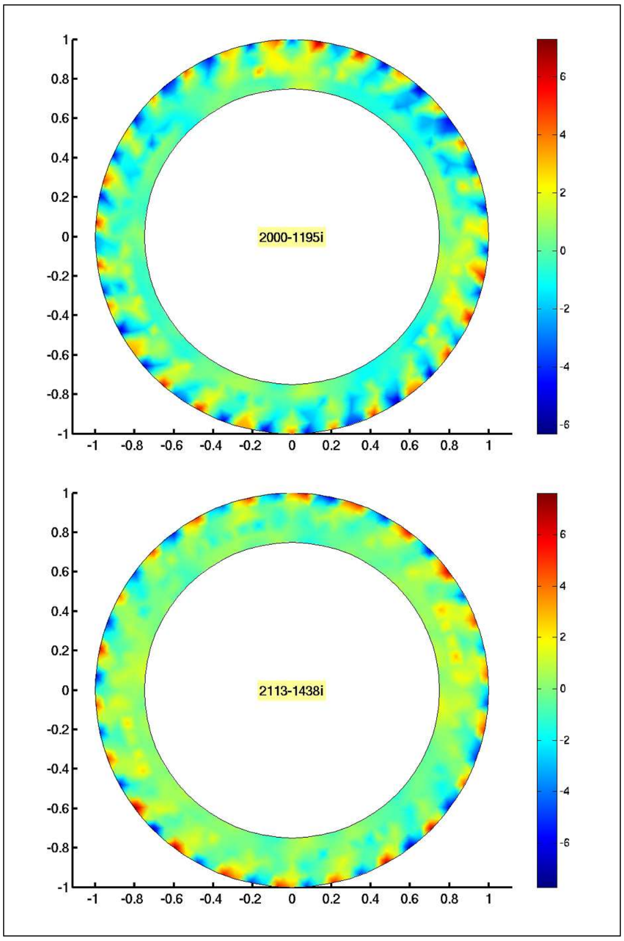

Figure 25. Sound pressure component of two spurious modes for $Ma = 0.1$; eigenvalue shown in the center of the annulus.

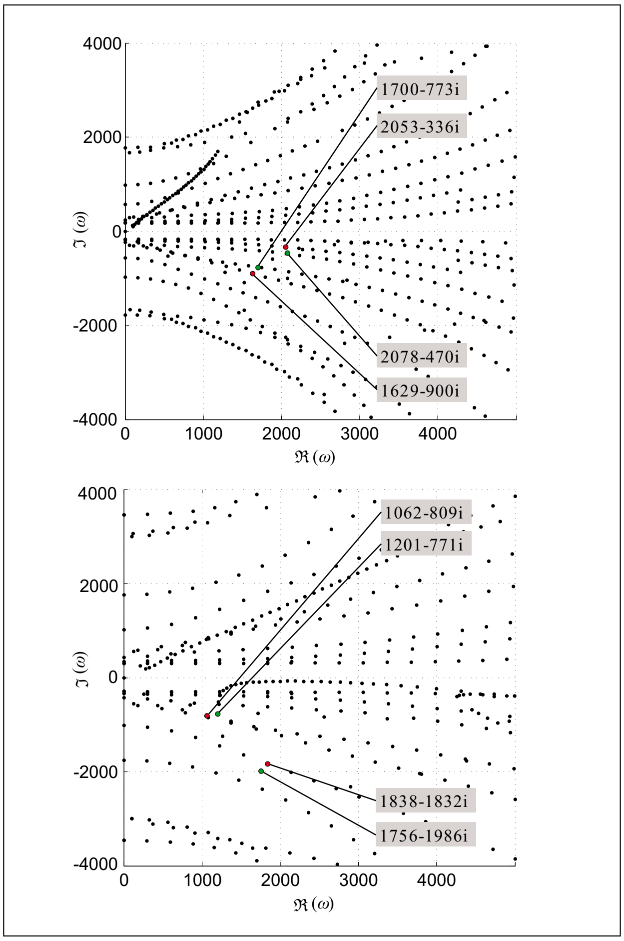

Figure 26. Eigenvalue distribution for $Ma = 0.5$ (top) and $Ma = 0.9$ (bottom).

the no-flow case, there are always spurious modes in the system. A problem with purely real eigenvalues or eigenvalues with a small imaginary part can be safely analyzed in the frequency domain since the physical and spurious modes are well separated from each other. This explains why Taylor-Hood elements have produced reliable solutions in literature.

An energy conserving shear flow problem of an annulus showed a similar eigenvalue distribution as the first example. Rotational modes have been identified as spurious modes. Vorticity modes as predicted in the literature could not be found. Acoustic modes proved to be real and well separated from the spurious modes.

The situation is different for exterior problems. The configuration of the annulus with an absorbing boundary is similar to that of an exterior problem, which is confirmed by the shape of the modes in the no-flow case. Again, Taylor-Hood elements produce spurious modes except for the no-flow case. Different from the duct example, physical and spurious modes can hardly be separated now. For a simple case as herein discussed, it seems possible to identify physical modes manually. Such a spatial filter technique could even be automated. However, it cannot account for a reasonable solution of exterior problems of the Galbrun equation, because evaluation of a large number of eigenvalues for real applications is not realistic.

The main conclusion is the need of developing a suitable finite element satisfying the inf-sup condition and is spurious modes free.

Acknowledgments

Three authors (F.D., R.R, and H.W.) were supported by BASAL project at the CMM, Universidad de Chile, Chile and Anillo ANANUM, ACT1118, CONICYT, Chile. Furthermore, traveling activities of three authors (F.D., L.H.-N., and S.M.) were supported by PPP – Acciones Integradas Hispano-Alemanas of the German Academic Exchange Service (DAAD) and the Spanish Ministry of Science.

References

[1] H. H. Brouwera, S. W. Rienstra: Aeroacoustics research in europe: The ceas-asc report on 2007 highlights. Journal of the Acoustical Society of America **318** (2008) 625–654.

[2] R. J. Astley: Numerical methods for noise propagation in moving flows with application to turbofan engines. Acoustical Science and Technology **30** (2009) 227–239.

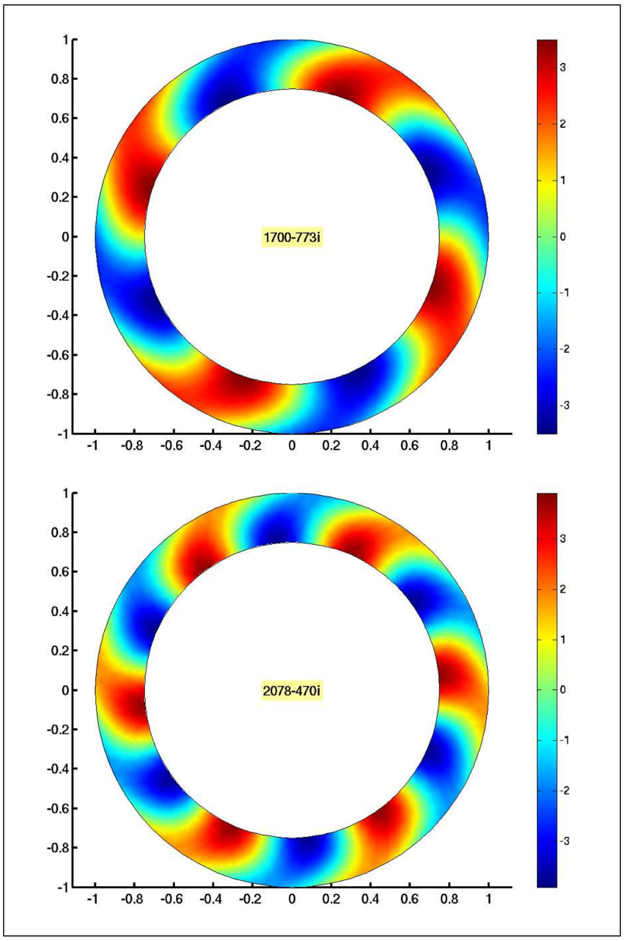

Figure 27. Sound pressure component of two physical modes for $Ma = 0.5$; eigenvalue shown in the center of the annulus.

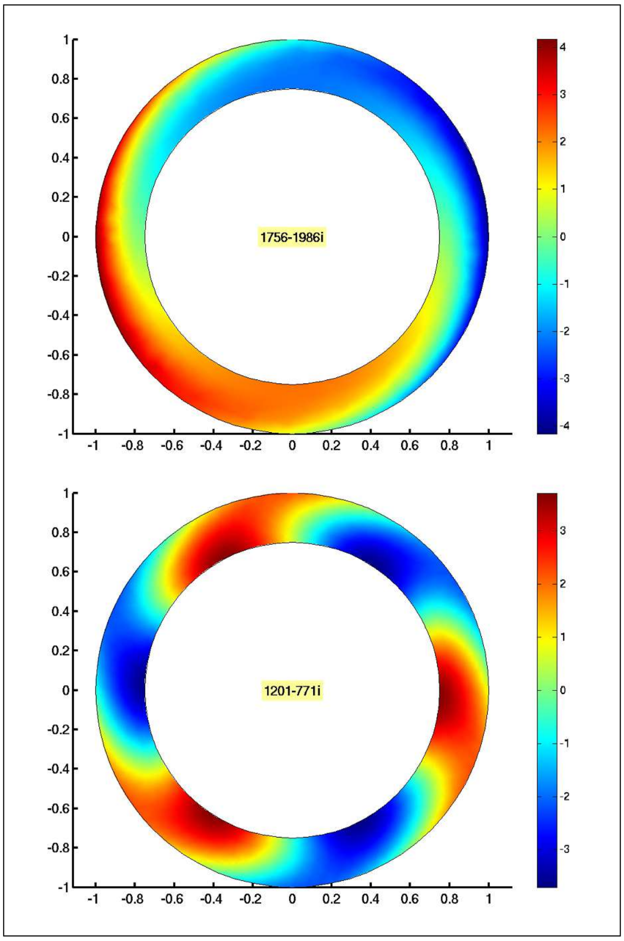

Figure 28. Sound pressure component of two physical modes for $Ma = 0.9$; eigenvalue shown in the center of the annulus.

[3] C. Bailly, D. Juve: Numerical solution of acoustic propagation problems using linearized euler equations. AIAA Journal **38** (2000) 22–29.

[4] G. Gabard: Discontinuous Galerkin methods with plane waves for time-harmonic problems. Journal of Computational Physics **225** (2007) 1961–1984.

[5] A. Hüppe: Spectral finite elements for acoustic field computations. Dissertation, Alpen-Adria Universität Klagenfurt, 2013.

[6] R. Ewert, W. Schröder: Acoustic perturbation equations based on flow decomposition via source filtering. Journal of Computational Physics **188** (2003) 365–398.

[7] A. Hüppe, M. Kaltenbacher: Spectral finite elements for computational aeroacoustics using acoustic perturbation equations. Journal of Computational Acoustics **20** (2012) 1240005–1–13.

[8] H. Galbrun: Propagation d'une onde sonore dans l'atmosphére et théorie des zones de silence. Gauthier-Villars, Paris, 1931.

[9] O. A. Godin: Reciprocity and energy theorems for waves in a compressible inhomogteneous moving fluid. Wave Motion **25** (1997) 143–167.

[10] G. Gabard, F. Treyssède, M. Ben Tahar: A numerical method for vibro-acoustic problems with sheared mean flows. Journal of Sound and Vibration **272** (2004) 991–1011.

[11] A. Minotti, J.-P. Brazier, F. Simon: Extension of the eulerian-lagrangian description to nonlinear perturbations in an arbitrary inviscid flow. Journal of Sound and Vibration **331** (2012) 4537–4553.

[12] F. Treyssède, M. Ben Tahar: Comparison of a finite element model with a multiple-scales solution for sound propagation in varying ducts with swirling flows. Journal of the Acoustical Society of America **115** (2004) 2716–2730.

[13] G. G. F. Treyssède, M. Ben Tahar: A mixed finite element method for acoustic wave propagation in moving fluids based on an eulerian-lagrangian description. Journal of the Acoustical Society of America **113** (2003) 704–716.

[14] C. Peyret, G. Élias: Finite-element method to study harmonic aeroacoustics problems. Journal of the Acoustical Society of America **110** (2001) 661–668.

[15] G. Gabard, R. J. Astley, M. Ben Tahar: Stability and accuracy of finite element methods for flow acoustics. I: General theory and application to one-dimensional propagation. International Journal for Numericals Methods in Engineering **63** (2005) 947–973.

[16] G. Gabard, R. J. Astley, M. Ben Tahar: Stability and accuracy of finite element methods for flow acoustics. II: Two-dimensional effects. International Journal for Numericals Methods in Engineering **63** (2005) 974–987.

[17] B. Nennig, E. Perrey-Debain, M. B. Tahar: A mode matching method for modelling dissipative silencers lined with poroelastic materials and containing mean flow. Journal of the Acoustical Society of America **128** (2010) 3308–3320.

[18] B. Nennig, M. B. Tahar, E. Perrey-Debain: A displacement-pressure finite element formulation for analyzing the sound

transmission in ducted shear flows with finite poroelastic lining. Journal of the Acoustical Society of America **130** (2011) 42–51.

[19] J.-P. Brazier: Derivation of an exact energy balance for galbrun equation in linear acoustics. Journal of Sound and Vibration **330** (2011) 2848–2868.

[20] S. Fuß, S. Hawkins, S. Marburg: An eigenvalue search algorithm for the modal analysis of a resonator in free space. Journal of Computational Acoustics **19** (2011) 95–109.

[21] A. Richter, J. Stiller, R. Grundmann: Stabilized discontinuous galerkin methods for flow-sound interaction. Journal of Computational Acoustics **15** (2007) 123–143.

[22] B. Poirée: Les équations de l'acoustique linéaire et nonlinéaire dans les fluides en mouvement. Acustica **57** (1985) 5–25.

[23] A. D. Pierce: Wave equation for sound in fluids with unsteady inhomogeneous flow. Journal of the Acoustical Society of America **87** (1990) 2292–2299.

[24] COMSOL Multiphysics Scripting Guide, version 3.5. COMSOL AB, Stockholm, Sweden, 2008.

[25] MATLAB Reference guide, version 7.6.0. The MathWorks, Inc., Natick, Massachusetts, 2008.

[26] O. C. Zienkiewicz, R. L. Taylor: The finite element method. Volume 1: The basis. 5 edition. Butterworth-Heinemann, Oxford, 2000.

[27] K.-J. Bathe: Finite element procedures. Prentice Hall, 1996.

[28] A.-S. Bonnet-Ben Dhia, G. Legendre, E. Luneville: Analyse mathematique de l'equation de galbrun en ecoulement uniforme. Comtes Rendus Académie des Sciences Paris, Serie IIb **329** (2001) 601–606.

[29] A.-S. Bonnet-Ben Dhia, E. M. Duclairoir, G. Legendre, J. Mercier: Time-harmonic acoustic propagation in the presence of a shear flow. Journal of Computational and Applied Mathematics **204** (2007) 428–439.

[30] A.-S. Bonnet-Ben Dhia, J.-F. Mercier, F. Millot, S. Pernet: A low mach number model for time-harmonic acoustics in arbitrary flows. Journal of Computational and Applied Mathematics **234** (2010) 1868–1875.

[31] H. Beriot: Elements finis d'ordre eleve pour l'operateur de Galbrun en regime harmonique. Dissertation, Universite Technologique de Compiegne, 2008.

[32] S. Marburg: Normal modes in external acoustics. Part I: Investigation of the one-dimensional duct problem. Acta Acustica united with Acustica **91** (2005) 1063–1078.

[33] H. Weisbecker: Numerical evaluation of the acoustic eigenvalue problem with present ambient flow velocity. Großer beleg, Technische Universität Dresden and Universidad de Concepción, 2009.
www.ing-mat.udec.cl/˜rodolfo/Tesis/Beleg-Hannah.pdf.

[34] F. Dietzsch: Numerical investigations for sound propagation in moving media. Diploma thesis, Technische Universität Dresden and Universidad de Concepción, 2011.
www.ing-mat.udec.cl/˜rodolfo/Tesis/Diploma-Felix.pdf.

[35] S. Marburg: Six boundary elements per wavelength. Is that enough? Journal of Computational Acoustics **10** (2002) 25–51.

[36] F. Ihlenburg: Finite element analysis of acoustic scattering. Springer, Berlin Heidelberg New York, 1998.

[37] S. Retka, S. Marburg: An infinite element for the solution of galbrun equation. Zeitschrift für Angewandte Mathematik und Mechanik **93** (2013) 154–162.

[38] S. Marburg, F. Dienerowitz, T. Horst, S. Schneider: Normal modes in external acoustics. Part II: Eigenvalues and eigenvectors in 2D. Acta Acustica united with Acustica **92** (2006) 97–111.

[39] S. Hein, T. Hohage, W. Koch: On resonances in open systems. Journal of Fluid Mechanics **506** (2004) 255–284.

[40] S. Hein, W. Koch, L. Nannen: Fano resonances in acoustics. Journal of Fluid Mechanics **664** (2010) 238–264.

[41] H. Peters, N. Kessissoglou, S. Marburg: Modal decomposition of exterior acoustic-structure interaction. Journal of the Acoustical Society of America **133** (2013) 2668–2677.

[42] O. Steinbach, G. Unger: A boundary element method for the Dirichlet eigenvalue problem of the Laplace operator. Numerische Mathematik **113** (2009) 281–298.